

# AD-A255 681



## REPORT DOCUMENTATION PAGE

Form Approved  
OMB No. 0704-0188

Public reporting burden for this collection of information is estimated to average 1 hour per response, including the time for reviewing instructions, searching existing data sources, gathering and maintaining the data needed, and completing and reviewing the collection of information. Send comments regarding this burden estimate or any other aspect of this collection of information, including suggestions for reducing the burden, to Washington Headquarters Service, Directorate for Information Operations and Reports, 1215 Jefferson Davis Highway, Suite 1204, Arlington, VA 22202-4302, and to the Office of Management and Budget, Paperwork Reduction Project (0704-0188), Washington, DC 20503.

1. AGENCY USE ONLY (Leave blank)	2. REPORT DATE 07.15.92	3. REPORT TYPE AND DATES COVERED Final report: 05.15.89 - 05.14.92
----------------------------------	----------------------------	---

4. TITLE AND SUBTITLE (U) PARTICLE DISPERSION IN A TURBULENT SHEAR FLOW	5. FUNDING NUMBERS PE - 61102F PR - 2308 TA - BS G - AFOSR 89-0392
--	--

6. AUTHOR(S) Ian M. Kennedy and Wolfgang Kollmann
--

7. PERFORMING ORGANIZATION NAME(S) AND ADDRESS(ES) Mechanical, Aeronautical and Materials Engineering University of California, Davis Davis, CA. 95616	8. PERFORMING ORGANIZATION REPORT NUMBER AFOSR-TR-92-0873
---	--

9. SPONSORING/MONITORING AGENCY NAME(S) AND ADDRESS(ES) AFOSR/NA Building 410 Bolling AFB DC 20332-6448	10. SPONSORING/MONITORING AGENCY REPORT NUMBER
--	--

11. SUPPLEMENTARY NOTES
-------------------------

DTIC  
S ELECTE D  
SEP 23 1992  
A

12a. DISTRIBUTION/AVAILABILITY STATEMENT Approved for public release; distribution is unlimited  92 9 22 095	12b. DISTRIBUTION CODE
---	------------------------

13. ABSTRACT (Maximum 200 words) A joint experimental and computational study of droplet dispersion in a round turbulent jet was carried out. Truly Lagrangian measurements of droplet dispersion were obtained with a laser scattering method. A low noise, high frequency response photomultiplier tube was used to track the location of particles as they traversed a sheet of laser light. Measurements of a single droplet at many closely spaced axial locations were obtained and were analyzed in terms of droplet times of flight to give Lagrangian statistics. The computational phase of the project consisted of stochastic simulations of droplet dynamics using the velocity statistics provided by a second order closure model for the jet flow, vortex dynamics for the initial region of the jet at infinite Reynolds number and finally a large eddy simulation method for the jet flow at finite Reynolds numbers. The droplet trajectories were computed to second order accuracy in each case. The large eddy simulation of a jet at a Reynolds number of 15,000 using the discretization error as filter showed very good results up to forty diameters downstream.
---

14. SUBJECT TERMS Turbulent shear flows, particle dispersion, vortex dynamics, stochastic simulation, large eddy simulation.	15. NUMBER OF PAGES 43
	16. PRICE CODE

17. SECURITY CLASSIFICATION OF REPORT Unclassified	18. SECURITY CLASSIFICATION OF THIS PAGE Unclassified	19. SECURITY CLASSIFICATION OF ABSTRACT Unclassified	20. LIMITATION OF ABSTRACT UL
---	--	---	----------------------------------

92-25664  
44  
NF  
07200



# PARTICLE DISPERSION IN A TURBULENT SHEAR FLOW

AFOSR Grant No. 89-0392

Final Report: 5/15/89 to 5/14/92.

Principal investigators: I.M. Kennedy and W. Kollmann

MAME Department, University of California at Davis, CA 95616

## Table of contents.

1.0	Summary of Research Progress.	3
1.1	Experimental Approach.	4
1.2	Computational Approach.	9
1.2.1	Stochastic Simulation.	9
1.2.2	Vortex Dynamics.	13
1.2.3	Large Eddy Simulation.	19
1.3	References	33
2.0	Personnel.	35
3.0	Publications.	35
4.0	Presentations.	35
5.0	Interactions.	35
	Inventions.	36
	Appendix	37

Accession For		
NTIS	CRA&I	↓
DTIC	TAC	<input type="checkbox"/>
Unannounced		<input type="checkbox"/>
Justification		
By		
Distribution		
Availability Codes		
Dist	Avail and/or	
	Special	
A-1		

DTIC QUALITY INSPECTED 3

## 1.0 Summary of Research Progress.

### Experiment.

An experimental technique has been developed to measure droplet dispersion and velocity statistics. Collection of statistically large sample sizes is facilitated by digital data acquisition. The experimental difficulty in tracking individual particles has been overcome using laser sheets and a position sensitive photo multiplier tube. Monodisperse droplets are injected onto the centerline of an air jet and their radial displacement is measured as a function of axial position. Direct measurements of particle velocity are obtained using thinly spaced parallel sheets of light. Time of flight, from the exit of the jet nozzle to the laser sheet, is measured for each particle. From these measurements dispersion rates (and particle diffusivities) are obtained. Measurements of droplet size, based on a slide impaction technique, allow mean vaporization rates to be measured.

Droplets have been generated from hexadecane, water and pentane, the later of which is volatile at room temperature. Hollow glass beads have also been utilized. Dispersion and vaporization are compared for droplets in an isothermal room temperature jet and from a heated jet ( $60^{\circ}C$ ) into room temperature air.

Radial displacement, axial velocity, axial velocity autocorrelation functions and time of flight are measured and compared to simulations. For droplets with large inertia relative to the turbulence, the initial conditions and early droplet displacement history have a significant effect on the downstream dispersion and particle diffusivity. Interactions with turbulence control the dispersion process for droplets less than  $\sim 50 \mu m$ . Axial velocity fluctuations and vaporization rates are underpredicted by the stochastic simulations. A comparison with a stochastic simulation of vaporizing particles suggests that the mass transfer and drag models may not be entirely satisfactory in a turbulent flow.

### Theory and Computation.

The flow field in turbulent round jets and the paths of droplets ranging from zero mass (fluid material points) to heavy particles (hexadecane droplets) are calculated numerically with several levels of sophistication.

The first method for the numerical simulation is based on a second order closure model for the jet turbulence and a stochastic simulation for the particle trajectories. Results are presented for a range of particle sizes from  $35 \mu m$  to  $160 \mu m$ , covering a range of particle response times from  $3ms$  to  $50ms$ . A typical fluid response time is  $18ms$  at an axial downstream distance of  $x/D = 40$ , based on results from the second order closure scheme. The jet Reynolds number is nominally 15,000, based on a nozzle diameter of  $7mm$ , and hot wire measurements indicate the turbulence is fully developed.

The second method is based on three-dimensional vortex dynamics for the simulation of the turbulent flow field at nominally infinite Reynolds number and numerical integration of the particle equations for the trajectories of the particles. Vortex rings are released at the jet pipe exit and their interaction and convective transport provides the velocity field for the particle dynamics. The interacting vortex filaments stretch each other and the number of discrete elements representing them increases rapidly as time evolves. Thus a limit for the simulation is reached at about eight to ten jet pipe diameters.

The drawbacks of the vortex dynamics approach lead to the third method. Highly accurate finite-difference methods were developed for the Large Eddy Simulation of the

flow fields in turbulent round jets. The dynamics of particles released at the nozzle center are calculated numerically and their statistical properties compared to measurements. The unsteady turbulent flow field can be calculated down to 40 diameters.

### 1.1 Experimental Approach.

This section of the report outlines the novel experimental technique that was developed to measure particle displacement and velocity. The measurements can yield either Lagrangian or Eulerian statistics of displacement and velocity. Single particles are tracked from a known initial location, and the time of flight is known for each particle.

In this study the droplet mass fraction is of the order  $10^{-6}$ . The droplets are separated by more than 1000 droplet diameters; hence, the droplets are non-interacting and have a negligible effect on the gas phase flow properties. The vaporization of hexadecane droplets in air at  $60^{\circ}C$  or less is negligible over the times of flight under investigation (typically less than  $50ms$ ).

A steady stream of monodisperse droplets is generated using a piezoelectric transducer. The droplets are accelerated by the air flow in the nozzle contraction. As each droplet passes from the nozzle, it intercepts a He-Ne laser beam which is monitored by a photo-diode. The diode signal is used as a trigger for the data acquisition system, and thus allows the time of flight to be measured for each droplet.

As the droplet travels axially downstream, it is radially displaced by the jet turbulence; the displacement from the jet axis is measured. The experimental difficulty in tracking individual particles from a known initial point has been overcome using a sheet of laser light and a position-sensitive photomultiplier tube (pmt). Droplet dispersion statistics are computed from the position measurements. For the present study, results are obtained for a jet Reynolds number of 15,000 based on a jet nozzle diameter of 7 mm. The axial distance from the tip of the jet nozzle to the laser sheet is variable as the jet nozzle and droplet or particle generation equipment are mounted on a motor driven slide mechanism.

The droplet size is governed by a glass nozzle attached to the transducer. A series of nozzles are fabricated from 1/8 inch hollow Pyrex rods. A rod can be heated and stretched, causing a waist to form in the region of stretching. Depending on the degree of stretching applied, the rod may no longer be hollow at this waist. The rod is then split at its narrowest point and both halves can be used as nozzles. The final step is to grind the tip smooth with sand paper. Depending on the extent of stretching and subsequent grinding, the orifice opening can vary from 15 to  $300 \mu m$ . For hydrocarbon fuels, the droplets are typically 30% larger than the orifice diameter.

A 514 nm Argon-ion laser beam, rated at 4W, is used to form a nominally 100 mm wide laser sheet using two cylindrical lenses. A polarization rotator can be used to rotate the polarization to yield the optimum signal to noise ratio. With the beam polarized horizontally, the quantity of light scattered from the droplets is maximized along with the quantity of Rayleigh scattered light from the air. This tends to maximize the signal-to-noise ratio since the signal strength increases more than the noise.

Light scattered from the droplets as they pass through the sheet is focused to a spot on a position sensitive detector by a collection lens. The photo-current signals from the detector are fed to operational-amplifier integrated circuits (op-amp) configured as current-to-voltage converters. Several types of detectors have been tested for use in the particle imaging. Three will be briefly described along with their relative advantages. The first detector investigated was a photo-diode with a square active area of  $100 mm^2$  and four

photo-current outputs- one on each side. Photodiodes are relatively inexpensive (this one costing  $\sim$  \$150), but the signal to noise ratio was prohibitably high for droplets less than  $150 \mu\text{m}$ . Additionally, the demagnification was relatively large: a viewing area of  $100 \text{ cm}^2$  (the laser sheet) was being imaged to a  $100 \text{ mm}^2$  active area. High demagnification ratios tend to increase the uncertainty contained in the calibration measurements as well as other sources of uncertainty such as the discretization error.

In an effort to reduce the noise, a second photodetector was tested. It has an active area of  $3 \text{ mm} \times 33 \text{ mm}$  and only two photo-current outputs: one on each end of the active surface. Thus, the detector can be used only for a one dimensional measurement of position. The magnification ratio was reduced from 10 to 3; but, since the active area is still  $100 \text{ mm}^2$ , the signal-to-noise ratio is equally poor compared to the first photo-diode.

Finally, a Hamamatsu position sensitive photomultiplier tube (pmt) was evaluated. The pmt has four outputs, one from each side of its square anode. The effective active area is  $1600 \text{ mm}^2$ , and the demagnification ratio is approximately two. The photomultiplier tube inherently has significantly less noise than the large active area photodiodes. This detector provides useful measurements for particles as small as  $35 \mu\text{m}$ . The only disadvantage of this detector is its relative cost:  $\sim$  \$2500.

The CAMAC data acquisition system incorporates two primary components: a clock and a data logger. The clock issues trigger pulses to the data logger, which samples the pmt signals each time a trigger is received.

A "burst mode" of data collection is used, whereby a fixed number, or burst of square wave pulses is issued by the clock to the data logger at a preset frequency each time a rising signal is received at the clock input. These clock output pulses are hard wired to the data logger, which takes a data sample each time a pulse is received. The data logger is configured to simultaneously record signals on a preset number of channels.

The data logger has 12 bit integer storage (i.e., 0 to 4,095 counts) corresponding to an input range of  $\pm 5.0$  volts. The electrical ground is assigned an integer value of 2,047. The data logger has storage capacity for 32,768 samples in the two memory modules connected to it.

A FORTRAN 77 data collection program was written to drive the CAMAC system. After initialization of the variables, the clock mode of operation is set to "burst mode". The number of pulses per burst is set along with the frequency of the pulses within each burst. Thus, each time a rising signal is received by the clock (i.e., a droplet passes through the He-Ne laser beam and is detected by the photo-diode), a string of data points is recorded.

The burst size and frequency are set so as to record data over a time period sufficient for the droplet to pass through the Argon-ion laser sheet. When the data logger's memory has been filled, the data logger is switched to "read" mode and the data are read out. The stream of integers is received by the PS/2 computer into an array and then stored as a data file on the hard drive. The data logger is then reset to "sweep and log" mode for more data collection. This process is repeated until the desired quantity of data is collected and stored.

The clock frequency is nominally set at 20 kHz. In the region near the nozzle, where the droplet velocity is high, a faster sampling rate is desirable. In this situation, it is useful to consider two channel data collection, since if only two channels are sampled, the maximum sampling frequency of the data logger is 50 kHz. With two channel data collection, the dispersion in the  $x_2$  or  $x_3$  direction can be measured, but not both simultaneously. The total data collection time is approximately 4 minutes per 1000 droplets. The droplets are

separated by more than 1000 droplet diameters; hence, the droplets are non-interacting and have a negligible effect on the gas phase flow properties. The vaporization of hexadecane droplets is negligible over the times of flight under investigation (typically less than 50 ms).

The time of flight for each particle is measured independently during the data collection. The number of counts between the center of the signal peak and droplet trigger signal divided by the CAMAC clock frequency yields the time of flight. If the clock frequency is 20 kHz, the time interval between data points is 0.05 ms. This time interval suggests an uncertainty two or three orders of magnitude less than the time of flight. A systematic error is introduced because the He-Ne laser beam is positioned slightly below the tip of the air jet nozzle (typically 1 mm). Since the particles are traveling 15 - 30 m/s, this error is also on the order of 0.05 ms.

### *Particle Velocity*

Axial droplet velocities are measured by timing the passage of droplets through the laser sheet. It is apparent that there is very little noise on the signal for 130  $\mu\text{m}$  droplets. Furthermore, the signal is approximated well by a Gaussian function as would be expected from an Argon-ion laser beam. The width of the pulse is proportional to the variance of the Gaussian curve fit,  $\sigma$ . This parameter is related, in turn, to the transit time of the droplet as it passes through the laser beam. Assuming the velocity gradients in the axial direction are not large, this time is inversely proportional to the droplet velocity. This has been calibrated by using the strobe light to time droplet motion over a measured distance.

The radial dispersion  $\sigma_r^2$  is computed using the following expression:

$$\sigma_r^2 = \frac{1}{n} \sum_{i=1}^n (x_{2,i}^2 + x_{3,i}^2)$$

where  $n$  is the number of droplet samples obtained and the  $x_{2,i}$  and  $x_{3,i}$  are the measured displacements from the jet axis for each droplet. The dispersion in the  $x_2$  or  $x_3$  direction is also readily computed:

$$\sigma_{x_2}^2 = \frac{1}{n} \sum_{i=1}^n x_{2,i}^2, \quad \sigma_{x_3}^2 = \frac{1}{n} \sum_{i=1}^n x_{3,i}^2$$

Since the flow field and dispersion are axisymmetric,  $\sigma_{x_2}^2 = \sigma_{x_3}^2$ . For experimental dispersion measurements, a total of 1000 droplets are used for statistics at each axial location downstream from the air jet nozzle. The radial displacement of a particle  $r_i = (x_{2,i}^2 + x_{3,i}^2)^{\frac{1}{2}}$  is a function of both the Eulerian variables  $t$  (time of flight) and  $x_3$  (axial distance). The time of flight and radial displacement is recorded for each droplet at a particular axial location.

### *Particle Sizing*

The droplet diameter can be measured by video micro-photography, with an estimated uncertainty of  $\pm 2\mu\text{m}$ . An alternative approach for droplet diameter measurement, precise only for non-vaporizing droplets, is to measure the droplet terminal velocity in quiescent air using the strobe light synchronization circuitry, an oscilloscope, and a small ruler (100 mm). The diameter of the glass particles is measured by collecting a sample of the particles exiting the jet and having them analyzed by the Facility for Advanced Instrumentation,

located on campus at UC Davis. They use a Cambridge Instruments QUANTIMET 900 particle sizer for this purpose. Of the sample analyzed, the mean particle diameter is  $60\mu\text{m}$ .

#### *Dispersion Results for Isothermal Non-vaporizing Droplets*

Particle displacement and time of flight statistics have been measured using a particle imaging method developed for this study. The statistics can be cast in an Eulerian or Lagrangian form since individual particles have been tracked from a known initial location, and each particle's time of flight is measured. The experiments have been simulated using a second order closure for the jet flow and a Lagrangian integration for particle trajectories.

The statistics are directly comparable to the droplet dispersion simulations. Simulations of particle dispersion have yielded good agreement with the experimental measurements provided that initial fluctuations in the radial velocity components are imposed so that the mean square particle velocity of the simulated droplets equals the observed velocity.

The droplets are far from equilibrium with the turbulence during the first  $30D$  due to mean slip between the particles and fluid. Slip decreases the interaction time between the particles and the surrounding fluid resulting in decreased dispersion.

The measurements of dispersion show the same limiting cases as do measurements from other types of flows. Dispersion grows quadratically in time early in the droplet history, then slows to a nearly linear growth rate. Beyond an axial distance of  $x_1/D = 30$ , the variance in time of flight begins to grow rapidly.

This study has highlighted the importance of specifying the initial conditions for particle trajectory, and in particular for droplets greater than about  $90\mu\text{m}$  because they possess sufficient inertia to be significantly far from equilibrium with the fluid in the rapidly evolving shear flow. As a consequence, the effect of the initial conditions at the nozzle exit may persist far downstream. This finding may be important with regard to modelling practical combustion sprays, where up to half of the fuel mass can be contained in droplets with significant inertia.

#### *Droplet Velocities and Correlations*

If the pair of coplanar sheets is redirected back through the flow field, a second measurement of the axial velocity is readily obtained. By collecting a large set of such measurements, it is possible to compute a two point axial velocity autocorrelation. The beam redirection is accomplished with a large right angle prism oriented with the largest face perpendicular to the incoming pair of laser sheets. A right angle prism used in this manner is often referred to as a retro-reflector. Retro-reflectors return the reflected light precisely coplanar with the incoming light, even if the prism is not oriented exactly perpendicular to the incoming light.

The following conclusion have been drawn:

1. The multiple sheet/position sensitive pmt diagnostic developed for this investigation can be used to measure particle velocities and correlations.
2. Hexadecane droplets of  $35\mu\text{m}$  or less follow the large scales of the flow. Particle Stokes numbers need to be less than 0.1, based on the Eulerian time scale for the particle to follow the integral fluctuations.
3. The stochastic simulation under predicts the integral length scales and the magnitude of the velocity fluctuations by a factor of two. This result could have considerable

importance in using this approach to model practical sprays.

### *Vaporizing Droplets*

This section presents experimental measurements and numerical simulations of droplet dispersion and time of flight within a round jet shear flow for heated ( $60^{\circ}\text{C}$ ) and unheated ( $20^{\circ}\text{C}$ ) air jets. The objective of the experiments is to compare the droplet interaction with the jet turbulence under two conditions:

- a) an isothermal room temperature air flowfield; and
- b) a  $60^{\circ}\text{C}$  air jet issuing into room temperature air.

Both vaporizing and non-vaporizing droplets are injected into both flows.

Pure n-pentane was used for the vaporizing liquid. Its normal boiling point is  $29^{\circ}\text{C}$ . Pure n-hexadecane, with a melting point of  $18^{\circ}\text{C}$  and a boiling point of  $287^{\circ}\text{C}$ , is not volatile at these temperatures. The isothermal case presents a situation in which the droplets experience unsteadiness only in the velocity field. In the heated jet, they experience an additional unsteadiness in the temperature field. The goal is determine the impact of the fluctuations on the droplet dispersion behavior. A technique using Polaroid film was used to estimate down stream droplet diameters for the pentane droplets. The film was exposed with no light providing a black print which was then cut into thin strips. At each axial location, a strip was attached to a thin rod and inserted into the flow, centered about the jet axis, for about 30 seconds. During that time roughly 40 droplets would strike the strip and etch its coating. The diameter of the etching is linear with the droplet diameter.

Droplet generation using pentane required the use of a thermo-electric cooling device to prevent vapor bubbles from forming inside the generator. The device was attached to an aluminum plate which surrounded the droplet generator. The thermoelectric cooler used a water heat exchanger for heat rejection. The device lowered the temperature of the pentane within the droplet generator to  $\sim -5^{\circ}\text{C}$ . The pentane reservoir level had to be carefully monitored to maintain a constant pressure head of about 1 mm pentane between the reservoir level and the lower tip of the droplet generation nozzle. Pentane is particularly sensitive to vibrations, loss of pressure head at the nozzle tip, and generator temperature variation, probably due to its lower viscosity and surface tension relative to hexadecane or water.

Data were obtained for hexadecane droplets of  $90\mu\text{m}$  and pentane droplets with nozzle exit diameters of  $113\mu\text{m}$ . The vaporizing droplets take longer to reach a given axial distance: as their diameter decreases, their inertia is reduced. This effect should be partially negated by the decrease in drag that results from the vaporization, but the data indicate that the vaporization effect is small.

The velocity measurements indicate that the peak velocity of the droplets in the heated jet is higher than the corresponding isothermal case. This behavior is due to the fact that the air jet velocity is higher at the nozzle exit and the droplet velocity shows a similar increase.

Simulations reproduce the mean velocity and time of flight statistics reasonably well. Some shortcomings of the stochastic simulations are apparent. First, the times of flight are underpredicted, implying that the drag coefficient may be too low. The same interpretation of the velocity data is applicable. The most interesting observation is that the relative positions of the two data sets are switched in the simulations. The data show indicate that the pentane droplets slow down more rapidly late in the flowfield (and have longer times of flight at a given axial location), but the simulations do not show this trend. It was found

that vaporization is not predicted accurately, and can account for the discrepancy.

The heated jet with pentane droplets had very strong dispersion, accentuated by the decrease in droplet size. This gives rise to a strongly varying dispersion rate throughout the flow domain. It may appear surprising that the hexadecane droplets in the heated jet disperse more rapidly than in the unheated jet. However, other researchers, such as Yuu, et al. (1978), have noted that dispersion scales with the absolute value of the initial velocity in the jet rather than the jet Reynolds number. The heated jet has a higher initial velocity and lower Reynolds number due to the increase in viscosity. The density variation is less than 1% beyond 20 jet diameters down stream.

Simulation of the pentane droplets show significant under prediction of the droplet vaporization, particularly in the heated jet case. Furthermore, the variance in droplet diameter is less than  $5 \text{ mm}^2$  for both cases at the downstream axial stations. The experiment had a much wider range. This result is obviously coupled to the under prediction of velocity fluctuations.

The results indicate the stochastic separated flow model used in these simulations, which neglects fine scale structure for the phase interaction, does a reasonably good job of predicting droplet drag, based on the observation that the mean profiles approximately agree. However, the agreement is not as encouraging for the calculations of heat and mass transfer to the droplet required for the prediction of vaporization rate. This result should be coupled to the under prediction of droplet velocity fluctuations.

Fine scale structure in the boundary layer of the droplets should have the effect of increasing heat transfer to the droplet and mass transfer away from it. Although it can not be determined unambiguously from the present study effects such as these would account for the differences between the measurements and the simulations; the evidence supports this conclusion.

## 1.2 Computational Approach.

### 1.2.1 Stochastic Simulation.

A second order closure model (Dibble et al., 1986), consisting of the transport equations for the mean velocity, the Reynolds stress components and the dissipation rate, is used to simulate the turbulent flow in the round jet. The model yields an Eulerian description of the turbulence statistics at single points and global scales for length and time in terms of the kinetic energy of turbulence and its dissipation rate. The mean and rms velocity components are specified at the particle location and the pdf of velocity is assumed to be Gaussian. The trajectory of each particle in the turbulent jet is marched in time by sampling the velocity pdf and solving the particle equations with a fourth-order accurate Runge-Kutta scheme. Three equations for the velocity components of a particle and three equations for its position were integrated simultaneously. If the particle is volatile, another equation for diameter is carried. If the flowfield has a temperature fluctuation imposed by heating the jet (which issues into ambient air), the local gas (or eddy) temperature is obtained from the simulated mixture fraction. It is assumed that the temperature field (or more appropriately, heat) is transported as a passive scalar such as mixture fraction. The local temperature is then found by sampling the mixture fraction pdf for a local value  $\zeta$ . The local eddy temperature  $T_e$  for nonreacting flow is then:  $T_e = \zeta(T_{jet} - T_{amb}) + T_{amb}$ .

A Lagrangian simulation of the droplet dispersion was then performed in the same manner as Faeth and co-workers (1985) by integrating the equations for particle motion

through the flow field. Three equations for the force components on a particle, with only drag and gravity considered, and three equations for its velocity were integrated simultaneously with a fourth order Runge-Kutta scheme to yield particle velocity and position:

$$\frac{d\vec{v}_p}{dt} = -\frac{3\rho_g C_D}{4d_p\rho_p}(\vec{v}_p - \vec{v}_g)|\vec{v}_p - \vec{v}_g| + \vec{g}$$

$$\frac{d\vec{x}_p}{dt} = \vec{v}_p$$

$C_D$  is the drag coefficient discussed below,  $\rho$  is the particle or gas density,  $\vec{v}$  is the particle or gas velocity,  $\vec{x}$  is the particle position,  $d_p$  is the droplet diameter, and  $\vec{g}$  is the acceleration due to gravity in the  $x_1$  direction.

For the simulations reported in this study, one thousand particles were simulated in each run to give representative statistics and the integration time step was 1 microsecond. The interaction of particles with the turbulence was simulated stochastically by randomly sampling the velocity pdfs, given the mean and variance of each flow velocity component as determined by the second order closure. The velocity pdfs were assumed to be Gaussian. Typical eddy length and time scales were estimated in the same manner as Shuen, et al. (1985) based on the dissipation length and time scales provided by the turbulence model:

$$L_e = C \frac{k^{1.5}}{\epsilon}, \quad \tau_e = \frac{L_e}{\sqrt{\frac{2\epsilon}{3}}}$$

$k$  is the turbulent kinetic energy and  $\epsilon$  is the dissipation rate.  $C$  is an semi-empirical coefficient set equal to 0.28 for all simulations in this study.

Use of this formulation implies that the interaction can be represented with only two turbulence scales. The interaction time for the droplet with the turbulent eddy was taken to be either the eddy lifetime or the transit time for the droplet to cross the eddy, whichever is shorter. The latter quantity was evaluated in the following manner. The distance that a droplet travels is tracked from the beginning of its interaction with an eddy. When this distance becomes greater than the eddy length scale, the flow velocity pdfs are sampled for new values.

Results of the simulations indicate that the eddy time scale rather than the length scale consistently constrains the interaction throughout the flow field. This result is apparently a deviation from simulations in grid turbulence. Such studies report that for light particles, such as hollow glass spheres transported in the grid turbulence of Snyder and Lumley (1971), the length scale should limit the interaction.

#### *Droplet Vaporization Model*

The mass vaporization rate  $\dot{m}_d$  is found from a mass balance:

$$\dot{m}_d = Sh \pi d_p \rho_g D_{AB} \frac{(Y_{F,s} - Y_{F,\infty})}{(1 - Y_{F,s})} = Nu \pi d_p \lambda_g \frac{(T - g - T_s)}{q_l}$$

where  $d_p$  is the droplet diameter,  $\lambda_g$  is thermal diffusivity,  $Nu$  is the Nusselt number,  $T_s$  is temperature at the droplet surface,  $q_l$  is the latent heat of vaporization,  $\rho_g$  is the gas density, and  $D_{AB}$  is the mass diffusivity of pentane in air,  $Y_F$  is the mass fraction at the

surface and in the free stream ( $Y_{F,\infty} = 0$ ). The heat and mass transfer numbers are defined by:

$$B_h = \frac{(T_g - T_s)}{q_l}, \quad B_m = \frac{(Y_{F,s} - Y_{F,\infty})}{(1 - Y_{F,s})}$$

and are used in the calculation of the Nusselt and Sherwood numbers, as well as the drag coefficient. The drag coefficient  $C_D$  recommended by Renksizbulut and Yuen (1983) includes a high Reynolds number correction to the Stokes formula that is important in modeling the behavior of the relatively large droplets as well as a correction for blowing:

$$C_D = \frac{24}{Re_p} (1 + 0.2 Re_p^{0.36}) (1 + B_h)^{-0.2}, \quad Re_p = \frac{\rho_g |\vec{v}_p - \vec{v}_g| d_p}{\mu_g}$$

$$Nu = 2 + 0.57 Re_p^{0.5} Pr^{0.33} (1 + B_h)^{-0.7}, \quad Pr = \frac{\lambda_g}{\rho_g C_p}$$

$$Sh = 2 + 0.57 Re_p^{0.5} Sc^{0.33} (1 + B_m)^{-0.7}, \quad Sc = \frac{\mu_g}{\rho_g D_{AB}}$$

$Re_p$  is the particle Reynolds number based on the droplet diameter, the relative velocity of the droplet and gas (eddy), and the gas kinematic viscosity. At each time step during the particle trajectory simulation, these equations are solved iteratively for the vaporization rate and the droplet surface temperature.

The droplet size change and temperature are then given by:

$$\frac{d(d_p)}{dt} = -2 \frac{\dot{m}_d}{\pi \rho_p d_p^2}$$

$$\frac{dT_s}{dt} = \frac{1}{\rho_p C_p} (Nu \pi d_p \lambda_g (T_g - T_s) - \dot{m}_d q_l)$$

The partial pressure of pentane at the droplet is used to calculate the mole fraction of pentane at the surface and is given by its surface temperature:

$$\frac{p_{F,s}}{P} = \chi_{F,s} = f(T_s)$$

$P$  is the absolute pressure (1 atm), and the function  $f$  is given by the Clausius-Clapeyron equation.

### *Jet and Droplet Scales*

The dispersion of heavy particles deviates from fluid particles for several reasons, all relating to the particles inertia. The droplets sizes which have been studied in this investigation cover a large range of response time scales and inertial effects are important. The droplet relaxation time that characterizes the particle inertia is based on terminal velocity and the gravitational constant, and is given by:

$$\tau_p = \frac{U_T}{g} = \left( \frac{4d_p(\rho_p - \rho_g)}{3C_D \rho_g g} \right)^{\frac{1}{2}}$$

$g$  is the gravitational acceleration constant,  $d_p$  is the particle diameter,  $\rho$  is the density of the particle or gas, and  $C_D$  is the drag coefficient given in the equation above, with the Reynolds number based on the droplet terminal velocity. Table 1 shows the scales for the droplets used in this investigation.

For Stokes flow, the time constant reduces to:

$$\tau_{p,St} = \frac{d_p^2 \rho_p}{18\mu_g}, \quad \rho_p \gg \rho_g$$

where  $\mu_g$  is the absolute viscosity of the fluid, in this case air, Table 1 shows the scales for a range of the droplets and particles used in this investigation.

Table I. Time scales of the air jet and droplets studied in this investigation.

Droplet Diameter ( $\mu m$ )	35	60	120	160
Terminal Velocity $U_T$ (m/s)	0.029	0.092	0.27	0.43
Terminal Reynolds Number $U_T d_p / \nu$	0.07	0.39	2.2	4.76
Response Time Constant $\tau_p$ (ms)	2.9	9.1	28.0	44.0
Turbulence Stokes Number $\tau_p / \tau_e^{(a)}$	0.16	0.51	1.6	2.4
Kolmogorov Stokes Number $\tau_p / \tau_K^{(b)}$	4.76	15	45	70
Acceleration Stokes at $x_1/D = 20$ :	0.17	0.55	1.67	2.63
Number $\tau_p / \tau_a^{(c)}$ at $x_1/D = 40$ :	0.043	0.14	0.42	0.66
Crossing Trajectories Ratio $U_T / v_{g,rms}^{(d)}$	0.03	0.1	0.3	0.5
Kolmogorov Length Scale at $x_1/D = 20$ :	1.38	1.53	3.06	4.08
Ratio $d_p / \eta_K$ at $x_1/D = 40$ :	0.69	0.76	1.53	2.04

(a)  $\tau_e = 18.0$  ms, obtained from the jet simulation at  $x_1/D = 40$ .

(b)  $\tau_K = 0.6$  ms, with  $\epsilon$  obtained from jet simulation at  $x_1/D = 40$ .

(c)  $\tau_a = 16.7$  ms at  $x_1/D = 20$  and 67 ms at  $x_1/D = 40$ .

(d)  $v_{g,rms} = 0.90$  m/s at  $x_1/D = 40$  on the jet axis from hot wire measurements.

The effect of inertia is relevant to these experiments and is related to the droplet response time: a heavy droplet will pass through an eddy if the instantaneous inertial force is considerably larger than the drag force. Due to mean slip between the particles and the flow, the interaction time between a particle and an eddy can be significantly decreased. This inertia effect is related entirely to mean velocities as opposed to velocity fluctuations and can be particularly important in free shear flows, since the gas mean velocity is continuously decreasing.

The relative importance of inertial effects can be deduced by comparing the ratio of a fluid time scale to the particle response time. If this ratio, or Stokes number, is greater than unity, the inertia significantly affects the droplet dispersion. These Stokes numbers are also provided, and as can be seen, for the flow conditions and particle sizes of this experiment, inertial effects can be important.

The Kolmogorov length scales at  $x_1/D = 20$  and 40 for a jet Reynolds number of 15,000 are estimated to be 39 and 78  $\mu m$ , respectively, using the relations given by Antonia et al. (1980). Because the smallest length scales of the turbulence are of the same order as the droplet diameters, it is possible that the turbulence may have an influence on the drag which is not predicted.

### 1.2.2 Vortex Dynamics.

The predominance of ring-like vortex structures in the transition region and possibly the fully turbulent region of the round jet suggests that this flow can be modelled by periodically releasing near the jet pipe exit vortex rings with small amplitude helical disturbances. A numerical simulation of this type of flow can be done in various ways but the presence of ring-like structures indicates that vortex dynamics offers the advantage of tracking the relevant parts of the fluid without requiring the discretization of the complete flow field (Chorin, 1980 and Leonard, 1985). The method developed for the present purpose is based on the inviscid Navier-Stokes equations written in terms of vorticity  $\vec{\omega}$  assuming constant density

$$\frac{D\vec{\omega}}{Dt} = (\vec{\omega} \cdot \nabla)\vec{v}$$

where the Stokes derivative is defined by

$$\frac{D}{Dt} \equiv \frac{\partial}{\partial t} + \vec{v} \cdot \nabla$$

The velocity  $\vec{v}$  follows from the relation

$$\Delta\vec{v} = -\nabla \times \vec{\omega}$$

and the solution of this Poisson equation can be given explicitly in the absence of boundaries. If the vorticity is concentrated in thin filaments, then the velocity induced by the filaments can be calculated from the Biot-Savart integral representing the solution of the Poisson equations for the velocity components. This integral is known to diverge for filaments of zero thickness and it follows that the internal structure of the filaments must be taken into account in order to obtain acceptable (convergent) values for the induced velocity. Several approximations are available (Chorin, 1980, Anderson and Greengard, 1985 and Leonard, 1985) for thin filaments. The method developed for the present purpose assumes thin filaments with circular cross-section and employs Rosenhead's method (Leonard, 1985 and Lundgren and Ashurst, 1989) where the integrand of the Biot-Savart solution is modified to remove the singularity according to

$$\vec{v}(\vec{x}, t) = -\frac{\Gamma}{4\pi} \int_C \frac{[\vec{x} - \vec{r}(s)] \times \frac{\partial \vec{r}}{\partial s}}{\{|\vec{x} - \vec{r}(s)|^2 + \mu^2\}^{\frac{3}{2}}} ds$$

The circulation of the filament is denoted by  $\Gamma$  and  $\vec{r}(s)$  is the position of the centerline  $C$  of the filament with arclength  $s$ . The parameter  $\mu > 0$  accounts for the internal structure of the filament in an approximate manner (Leonard, 1985). Moore (1972) showed that it should be proportional to the local core radius  $\sigma$

$$\mu = \alpha^{\frac{1}{2}} \sigma$$

where  $\alpha$  is a non-dimensional parameter which reflects the vorticity distribution in the core of the filament. For uniform vorticity distribution in the core  $\alpha \approx 0.22$  holds.

The thin filament approximation has several limitations. In particular, it predicts excessive growth rates for short wavelength disturbances and energy is not conserved if the filament cores overlap (Ashurst and Meiburg, 1988). It is able to simulate the dynamics

of inviscid flows as long as the filaments do not come too close to each other and create the excessive growth rates. It cannot represent the viscous reconnection phenomenon of filaments which is important for turbulent flows at high but finite Reynolds numbers. Therefore, the vortex dynamics scheme based on the thin filament approximation was used to represent the flow in the initial region of the jet.

#### *Particle dynamics.*

Fluid particles (fluid material points) and solid particles were considered. The fluid particles are essentially massless particles which move exactly with the fluid velocity. The Lagrangian position field for fluid material points requires integration of the kinematic relation between velocity and position. Thus, the integration of the fluid particle equations is straightforward. The kinematic relation between position  $\underline{X}$  and velocity  $\underline{V}$  is given by the system of odes

$$\frac{\partial X_\alpha}{\partial t}(\underline{a}, t) = v_\alpha(\underline{X}(\underline{a}, t), t)$$

with the initial conditions  $\underline{X}(\underline{a}, t) = \underline{a}$  ( $\underline{a}$  denotes the Lagrangian label variable defined by  $\underline{a} \equiv \underline{X}(\underline{a}, 0)$ ),  $\underline{v}(\underline{x}, t)$  is the Eulerian velocity). The Eulerian velocity field is given by the approximate form of the Biot-Savart law discussed in the previous section. The time integration is carried out simultaneously with the advancement of the vortex filaments using the second order accurate trapezoidal time integration. The dynamic equation determining the location of heavy particles is a consequence of Newton's second law with approximations for the forces acting on the particle (see Odar and Hamilton, 1964). The equation for the particle velocity contains terms representing drag and virtual mass, the Basset term and buoyancy.

$$\begin{aligned} \frac{d\underline{u}_p}{dt} = & \frac{3C_D}{4d} \frac{\rho_g}{\rho_p} |\underline{u}_g - \underline{u}_p| (\underline{u}_g - \underline{u}_p) + \frac{1}{2} \frac{\rho_g}{\rho_p} C_I \frac{D}{Dt_p} (\underline{u}_g - \underline{u}_p) + \frac{\rho_g}{\rho_p} \frac{D\underline{u}_g}{Dt_g} \\ & + \frac{9}{d} \frac{\rho_g}{\rho_p} \left( \frac{\nu}{\pi} \right)^{\frac{1}{2}} C_B \int_{t_0}^t \frac{d\tau}{(t-\tau)^{\frac{3}{2}}} \frac{D}{D\tau_p} (\underline{u}_g - \underline{u}_p) + \left( \frac{\rho_g}{\rho_p} - 1 \right) \underline{g} \end{aligned}$$

The subscript  $g$  denotes gas and  $p$  particle properties, the substantial derivatives are to be taken accordingly as following a material point or the particle,  $d$  is the particle diameter,  $\nu$  is the gas viscosity and  $\underline{u}_g$ ,  $\rho_g$  are taken as the values undisturbed by the particle at the location of the particle. The coefficients  $C_D$ ,  $C_I$  and  $C_B$  are in general functions of the particle Reynolds number

$$Re_p \equiv \frac{|\underline{u}_g - \underline{u}_p| d}{\nu}$$

and the acceleration number (see Faeth, 1983 and Hansell et al., 1992)

$$An \equiv \frac{\frac{D}{Dt_p} |\underline{u}_g - \underline{u}_p| d}{|\underline{u}_g - \underline{u}_p|^2}$$

The drag coefficient is given by (Putnam, 1961)

$$C_d = \frac{24}{Re} \left( 1 + \frac{Re_p^{\frac{1}{2}}}{6} \right) \quad \text{for } Re_p < 1000$$

The particle velocity is thus determined as solution of

$$\frac{d\mathbf{u}_p}{dt} = \frac{3}{4} \frac{C_D}{d} \frac{\rho_g}{\rho_p} |\mathbf{u}_g - \mathbf{u}_p| (\mathbf{u}_g - \mathbf{u}_p) + \frac{\rho_g}{\rho_p} \frac{D\mathbf{u}_g}{Dt} + \left( \frac{\rho_g}{\rho_p} - 1 \right) \mathbf{g}$$

For these calculations, the properties for  $d = 36 \mu m$  liquid hexadecane particles are used which are given by  $\rho_p = 775[\frac{kg}{m^3}]$ . The relevant properties of air are  $\nu = 1.45(10)^{-5}$ ,  $\rho_g = 1.19[\frac{kg}{m^3}]$ .

The dynamics of the flow field and the particles transported by it are illustrated in Fig.1 to Fig.3. The vortices are shown as lines (centerlines of the filaments) and the particles as circles. These pictures show how the vortices coalesce, the helical disturbances grow and the filaments entangle as time progresses. Three coalescing regions are present from  $0.5D$  to  $3.5D$ , which agrees with the observations made by Yule (1978). The first combination of ring structures occurs at approximately one diameter as shown in Fig.1 (upper graph). This group then combines with either one, two or three rings to form a group of 3 to 5 rings as illustrated by the groups centered at  $1.75D$  and  $1.5D$  in Fig.1 and Fig.2 (upper graphs). The final combination involves groups of 3 to 5 vortices and occurs between  $2D$  and  $3.5D$ . The large group located at  $3.5D$  in Fig.3 (upper graph) is the result of this last combination and corresponds to the puffs of smoke which were observed by Crow and Champagne (1971). The particles shown as circles in the figures show rapid acceleration in axial and radial direction but very little movement in azimuthal direction. The final coalescence of the vortex filaments and the large group of filaments formed during this process are primarily responsible for the radial dispersion of the particles. As the group of five rings at  $1.75D$  in Fig.1 passes through the rings at  $2.5D$ , it accelerates both axially and radially. A few of the particles are pulled along, as seen in Fig.2 at  $2.5D$ . Most are left behind, however, due to their inertial resistance to fluid accelerations, as indicated by the group of particles at  $3.0D$  in Fig.3. Since the fluid velocity in the region between the large groups of filaments is small, the group of particles at  $3.0D$  in Fig.3 will decelerate. This group will then be dispersed radially away from the jet by the group of filaments at  $2.0D$  in the same figure, like the group of particles currently at  $4.5D$ . From these observations a two-step process for particle dispersion in the transition region of round jets may be deduced. In the first step particles are stranded by the final coalescence of vortex rings in the regions with low velocity behind and in front of the coalescing filaments. These stranded groups of particles are then dispersed radially away from the centerline by the next group of filaments.

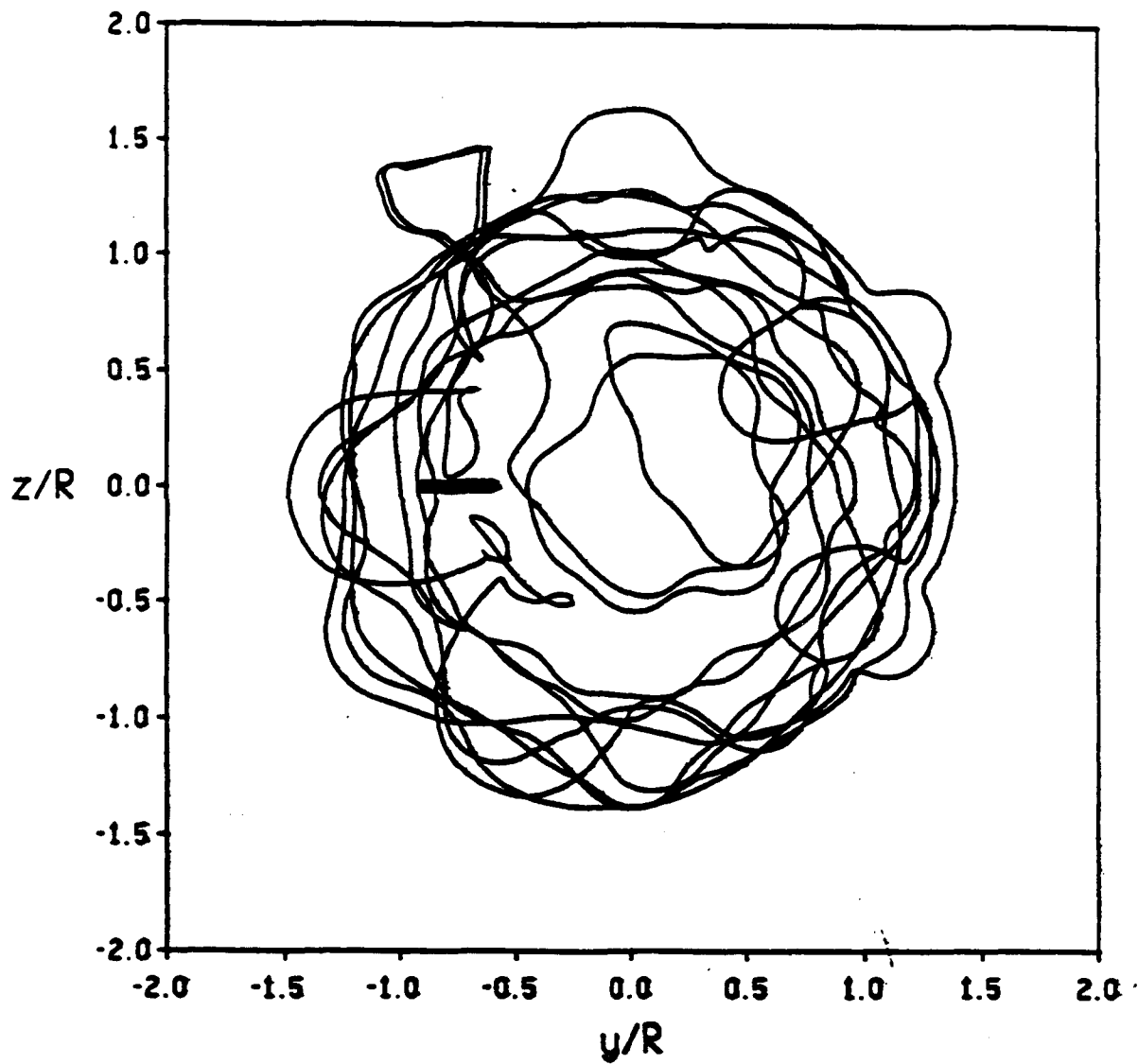
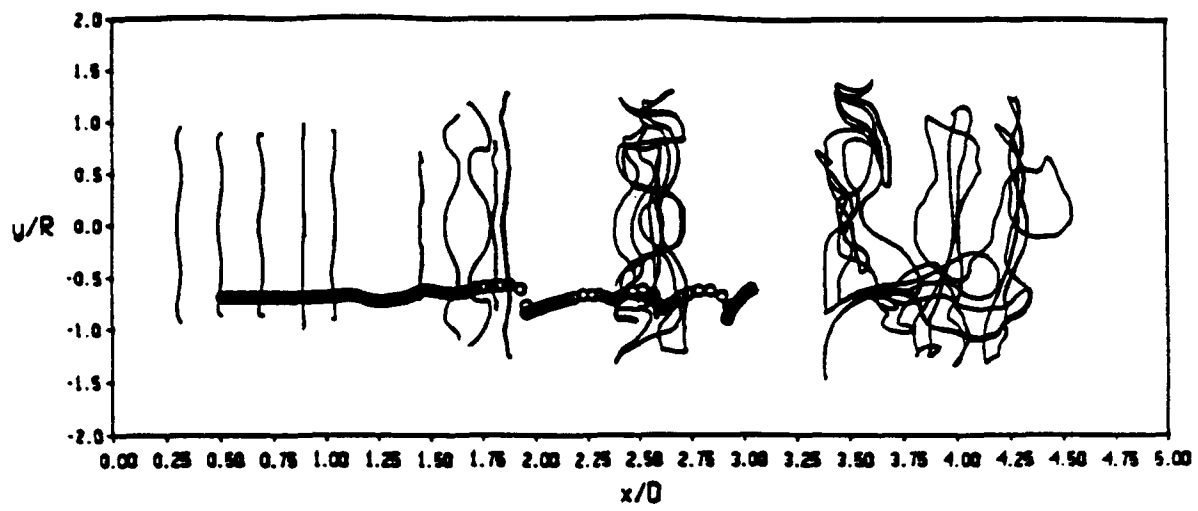


Fig.1 Centerlines of vortex filaments (lines) and circumferential and radial dispersion of rigid particles (circles,  $\rho = 700 \frac{\text{kg}}{\text{m}^3}$ ,  $d = 50 \mu\text{m}$ ) at  $p = 10^5 \text{ Pa}$ ,  $T = 300\text{K}$  and  $t=30.75$  dimensionless time units

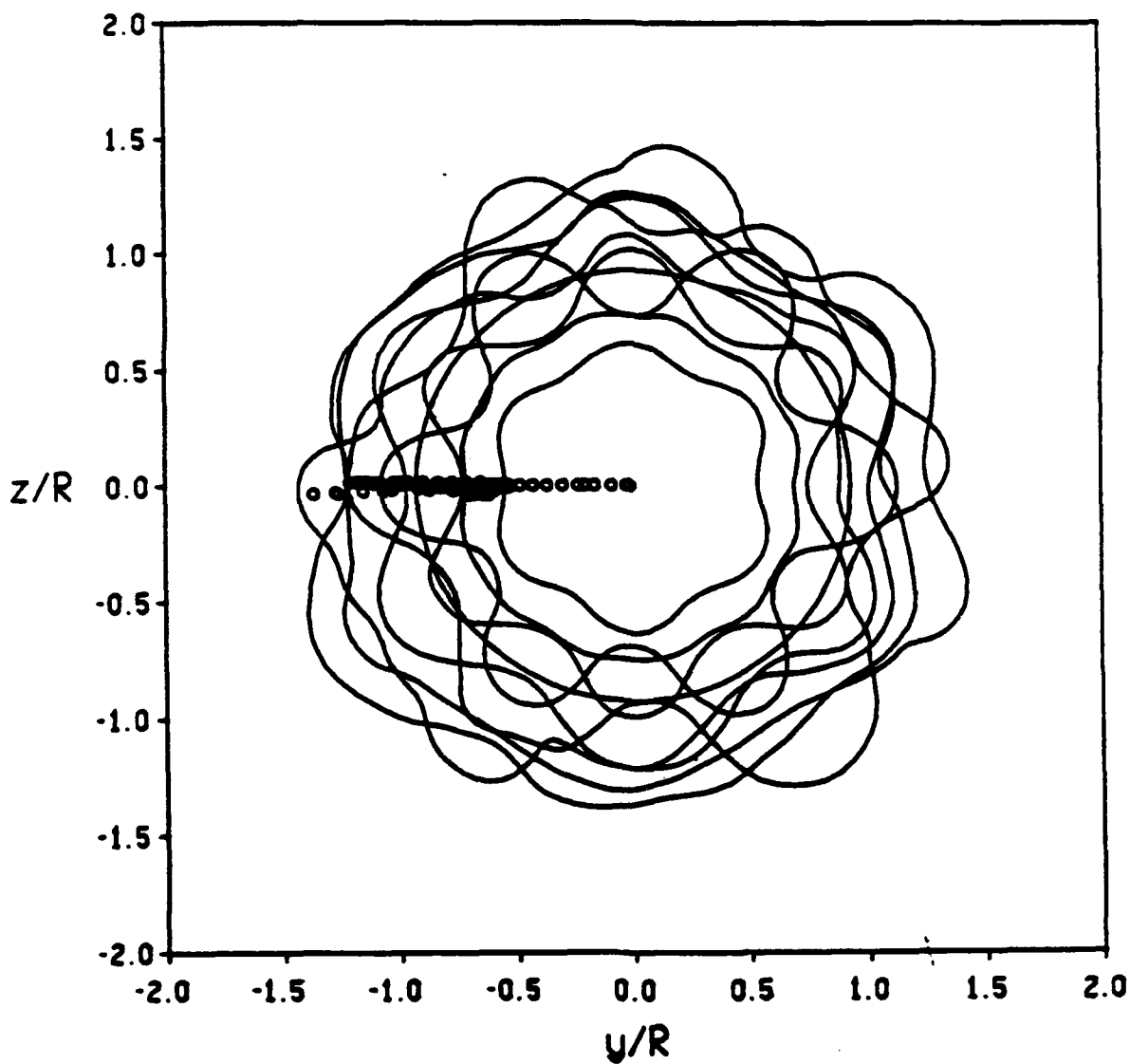
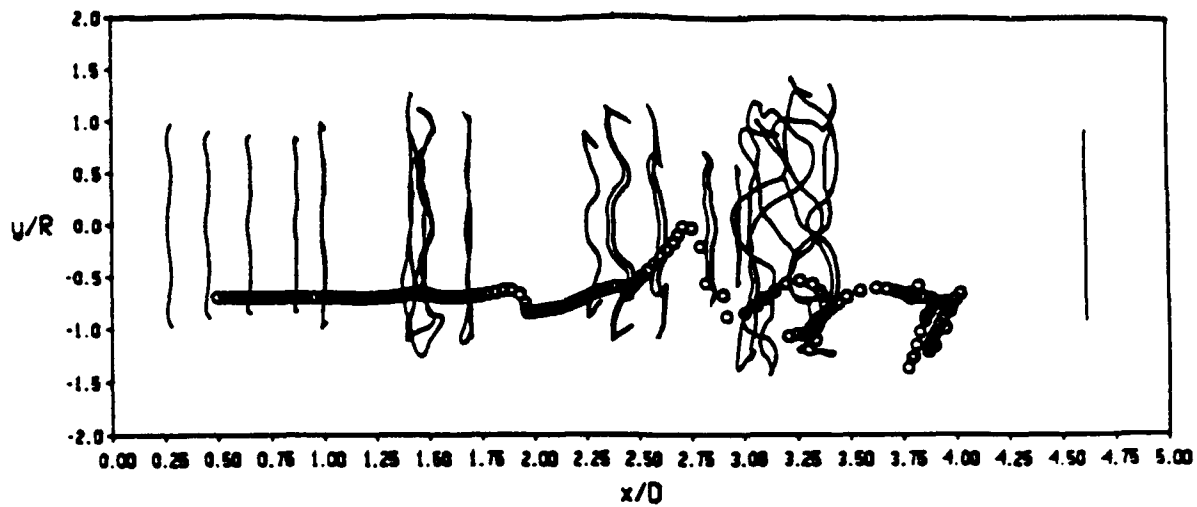


Fig.2 Centerlines of vortex filaments and circumferential and radial dispersion of rigid particles ( $\rho = 700 \frac{\text{kg}}{\text{m}^3}$ ,  $d = 50 \mu\text{m}$ ) at  $p = 10^5 \text{ Pa}$ ,  $T = 300 \text{ K}$  and  $t=33.77$  dimensionless time units

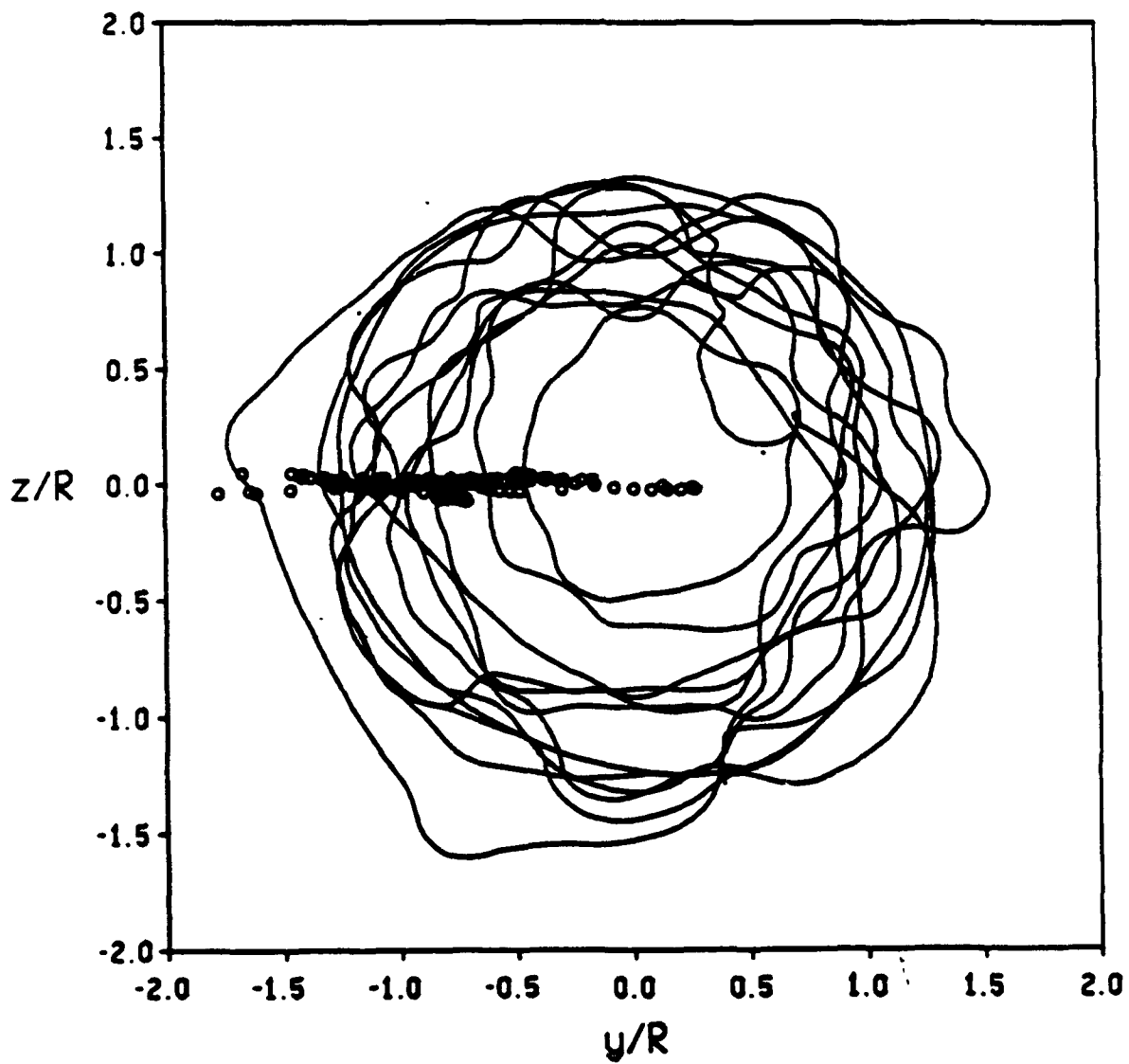
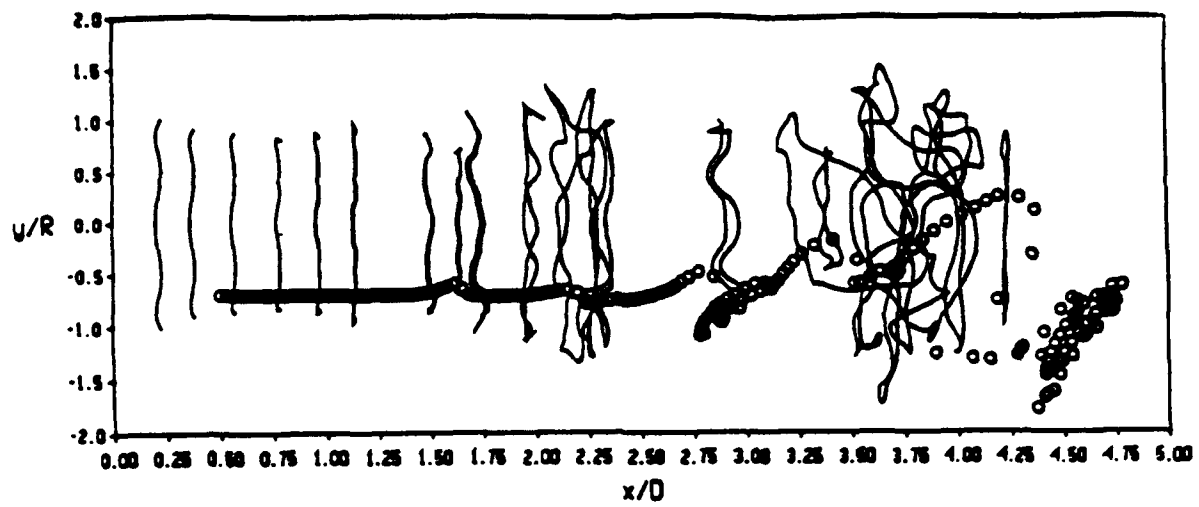


Fig.3 Centerlines of vortex filaments and circumferential and radial dispersion of rigid particles ( $\rho = 700 \frac{kg}{m^3}$ ,  $d = 50 \mu m$ ) at  $p = 10^5 Pa$ ,  $T = 300K$  and  $t=36.72$  dimensionless time units

### 1.2.3 Large Eddy Simulation.

The Large Eddy Simulation or Direct Numerical Simulation of the flow in turbulent round jets is the most realistic approach for the prediction of the flow field and the simulation of Lagrangian particle dynamics in this type of flow. The simulation of turbulent flow fields in round jets is based on highly accurate finite-difference methods, which offer the flexibility necessary for the treatment of non-periodic jet flows emitting from nozzles and the consideration of a variety of exit conditions. Furthermore, the influence of disturbances created at the jet pipe exit on the flow development can be studied in detail.

#### *Solution method.*

Mass and momentum balances are set up in cylindrical coordinates for the primitive variables velocity and pressure. Cylindrical coordinates  $(r, \theta, \zeta)$  are appropriate for circular jets. Stretched grids are used in the  $r$  and  $\zeta$  directions to concentrate the grid points in the region of interest and to remove the outer boundary as far as possible without wasting too many grid points. The grid stretching transformation allows the solution to be computed on a uniform mesh and then to be transformed onto the real (physical) mesh. The transformation is given by

$$\bar{\Psi} = 1 - \frac{\log \left\{ \frac{[\beta+1 - \frac{\Psi}{\Psi_{max}}]}{[\beta-1 + \frac{\Psi}{\Psi_{max}}]} \right\}}{\log \left( \frac{\beta+1}{\beta-1} \right)}$$

where  $\Psi$  represents either  $r$  or  $\zeta$  and  $\beta$  is the stretching parameter ( $\beta < 1$ ). The stretching is greatest for  $\beta \rightarrow 1$

The inverse transformation (which is what is actually used in practice) is then given by

$$\Psi = \Psi_{max} \frac{(\beta+1) - (\beta-1) \left[ \frac{\beta+1}{\beta-1} \right]^{1-\bar{\Psi}}}{\left[ \frac{\beta+1}{\beta-1} \right]^{1-\bar{\Psi}} + 1}$$

The derivatives of the above transformation can be calculated analytically as follows

$$\frac{\partial \bar{\Psi}}{\partial \Psi} = \frac{2\beta}{\Psi_{max} \{ \beta^2 - [1 - \frac{\Psi}{\Psi_{max}}]^2 \} \ln \left[ \frac{\beta+1}{\beta-1} \right]}$$

and the second derivative emerges as

$$\frac{\partial^2 \bar{\Psi}}{\partial \Psi^2} = \frac{-4\beta}{\Psi_{max}^2 \{ \beta^2 - [1 - \frac{\Psi}{\Psi_{max}}]^2 \}^2 \ln \left[ \frac{\beta+1}{\beta-1} \right]}$$

All derivatives are calculated in the transformed space and then brought back to real space via the transformation metrics using the chain rule as follows

$$\frac{\partial v}{\partial \Psi} = \frac{\partial v}{\partial \bar{\Psi}} \frac{\partial \bar{\Psi}}{\partial \Psi}$$

The transformation rules allow the set up of the Navier-Stokes equations in the stretched coordinates.

### Navier-Stokes equations in transformed space

The Navier-Stokes equations are made dimensionless as usual by using reference values for all variables based on the radius of the jet ( $r_{jet}$ ) and the average velocity of the jet at the pipe exit ( $v_{jet}$ ). Thus, the dimensionless variables are defined as follows (bars indicate nondimensional variables)

$$\bar{v}_r = \frac{v_r}{v_{jet}}; \quad \bar{v}_\theta = \frac{v_\theta}{v_{jet}}; \quad \bar{v}_\zeta = \frac{v_\zeta}{v_{jet}}$$

$$\bar{t} = \frac{tv_{jet}}{r_{jet}}; \quad \bar{\rho} = \frac{\rho}{\rho_{jet}} = 1; \quad (\text{for incompressible flows})$$

$$\bar{p} = \frac{p}{\rho v_{jet}^2}; \quad Re = \frac{r_{jet} v_{jet}}{\nu}$$

All variables will be nondimensional in the following and the bars can be dropped for convenience. (Note that the bars will hereafter indicate the transformed space).

The Navier-Stokes equations are transformed to the stretched coordinates. The starting point are the mass and momentum balances in cylindrical coordinates. Application of the stretching transformation to the mass balance leads to

$$\frac{1}{r} \frac{\partial \bar{r}}{\partial r} \frac{\partial}{\partial \bar{r}} (r v_r) + \frac{1}{r} \frac{\partial v_\theta}{\partial \theta} + \frac{\partial \bar{\zeta}}{\partial \zeta} \frac{\partial v_\zeta}{\partial \bar{\zeta}} = 0$$

The radial momentum balance in transformed coordinates is given by

$$\frac{\partial v_r}{\partial t} + v_r \frac{\partial \bar{r}}{\partial r} \frac{\partial v_r}{\partial \bar{r}} + \frac{v_\theta}{r} \frac{\partial v_r}{\partial \theta} + v_\zeta \frac{\partial \bar{\zeta}}{\partial \zeta} \frac{\partial v_r}{\partial \bar{\zeta}} - \frac{v_\theta^2}{r} = -\frac{1}{\rho} \frac{\partial \bar{r}}{\partial r} \frac{\partial p}{\partial \bar{r}} + \frac{1}{Re} \left\{ \left( \frac{\partial \bar{r}}{\partial r} \right)^2 \frac{\partial^2 v_r}{\partial \bar{r}^2} \right.$$

$$\left. + \left( \frac{1}{r} \frac{\partial \bar{r}}{\partial r} + \frac{\partial^2 \bar{r}}{\partial r^2} \right) \frac{\partial v_r}{\partial r} - \frac{v_r}{r^2} + \frac{1}{r^2} \frac{\partial^2 v_r}{\partial \theta^2} + \left( \frac{\partial \bar{\zeta}}{\partial \zeta} \right)^2 \frac{\partial^2 v_r}{\partial \bar{\zeta}^2} + \frac{\partial^2 \bar{\zeta}}{\partial \zeta^2} \frac{\partial v_r}{\partial \bar{\zeta}} - \frac{2}{r^2} \frac{\partial v_\theta}{\partial \theta} \right\}$$

The azimuthal momentum balance in transformed coordinates is given by

$$\frac{\partial v_\theta}{\partial t} + v_r \frac{\partial \bar{r}}{\partial r} \frac{\partial v_\theta}{\partial \bar{r}} + \frac{v_\theta}{r} \frac{\partial v_\theta}{\partial \theta} + v_\zeta \frac{\partial \bar{\zeta}}{\partial \zeta} \frac{\partial v_\theta}{\partial \bar{\zeta}} - \frac{v_\theta v_r}{r} = -\frac{1}{\rho r} \frac{\partial p}{\partial \theta} + \frac{1}{Re} \left\{ \left( \frac{\partial \bar{r}}{\partial r} \right)^2 \frac{\partial^2 v_\theta}{\partial \bar{r}^2} \right.$$

$$\left. + \left( \frac{1}{r} \frac{\partial \bar{r}}{\partial r} + \frac{\partial^2 \bar{r}}{\partial r^2} \right) \frac{\partial v_\theta}{\partial r} - \frac{v_\theta}{r^2} + \frac{1}{r^2} \frac{\partial^2 v_\theta}{\partial \theta^2} + \left( \frac{\partial \bar{\zeta}}{\partial \zeta} \right)^2 \frac{\partial^2 v_\theta}{\partial \bar{\zeta}^2} + \frac{\partial^2 \bar{\zeta}}{\partial \zeta^2} \frac{\partial v_\theta}{\partial \bar{\zeta}} + \frac{2}{r^2} \frac{\partial v_r}{\partial \theta} \right\}$$

Finally, the axial momentum balance is given by

$$\frac{\partial v_\zeta}{\partial t} + v_r \frac{\partial \bar{r}}{\partial r} \frac{\partial v_\zeta}{\partial \bar{r}} + \frac{v_\theta}{r} \frac{\partial v_\zeta}{\partial \theta} + v_\zeta \frac{\partial \bar{\zeta}}{\partial \zeta} \frac{\partial v_\zeta}{\partial \bar{\zeta}} = -\frac{1}{\rho} \frac{\partial p}{\partial \zeta} + \frac{1}{Re} \left\{ \left( \frac{\partial \bar{r}}{\partial r} \right)^2 \frac{\partial^2 v_\zeta}{\partial \bar{r}^2} \right.$$

$$\left. + \left( \frac{1}{r} \frac{\partial \bar{r}}{\partial r} + \frac{\partial^2 \bar{r}}{\partial r^2} \right) \frac{\partial v_\zeta}{\partial r} - \frac{v_\zeta}{r^2} + \frac{1}{r^2} \frac{\partial^2 v_\zeta}{\partial \theta^2} + \left( \frac{\partial \bar{\zeta}}{\partial \zeta} \right)^2 \frac{\partial^2 v_\zeta}{\partial \bar{\zeta}^2} + \frac{\partial^2 \bar{\zeta}}{\partial \zeta^2} \frac{\partial v_\zeta}{\partial \bar{\zeta}} \right\}$$

The next step is now the discretization of this system of nonlinear partial differential equations and the design of the solution algorithm.

### *Solution algorithm*

The difficulty with the above equations is that there is no explicit evolution equation for the pressure. The incompressibility constraint yields the continuity equation as given above but in practice this equation is not solved. Rather the momentum equations are first updated and the result is then "corrected" in order to satisfy conservation of mass. The effect of mass balance is essentially to modify the pressure field and this method is, therefore, termed a pressure correction method.

Since pressure is a phenomenon which acts at cell centers it does not generate fluid vorticity for incompressible flow. (Pressure can generate vorticity for compressible flow because it causes density differences between neighboring cells which can cause fluid rotation.) This implies that for incompressible flow the velocity correction field  $\underline{v}_c$  is irrotational and incompressible. It can be shown that for this case the velocity correction field can be represented as the gradient of a scalar

$$\underline{v}_c = -\nabla\phi$$

Mass balance is now enforced by carrying out the following steps. First the momentum balances are solved providing the intermediate solution  $\underline{v}^{n'+1}$ . Then the velocity is corrected in the following manner

$$\underline{v}^{n+1} = \underline{v}^{n'+1} + \underline{v}_c = \underline{v}^{n'+1} - \nabla\phi$$

In order to satisfy continuity at the new  $(n+1)$  time step we have

$$\nabla \cdot \underline{v}^{n+1} = \nabla \cdot (\underline{v}^{n'+1} - \nabla\phi) = 0$$

Thus a Poisson equation for the pressure correction variable  $\phi$  is obtained

$$\nabla \cdot \underline{v}^{n'+1} = \nabla^2\phi$$

Now, the equation for the pressure correction can be derived by substituting the above relation into the momentum equation. This step can be carried out if the time derivative is discretized. Hence, let the time derivative be discretized using the three point backward (Adams Bashforth) finite difference approximation. Writing the vector form of the momentum equations using explicit convective and diffusion terms yields

$$\frac{3(\underline{v}^{n'+1} - \nabla\phi) - 4\underline{v}^n + \underline{v}^{n-1}}{2\Delta t} + \underline{v}^n \cdot \nabla \underline{v}^n = -\frac{1}{\rho} \nabla(p^n + p_c) + \frac{1}{Re} \Delta \underline{v}^n$$

Subtracting from equation the explicit momentum equation update yields the following relation for the pressure correction  $p_c$ .

$$p_c = \frac{3}{2} \frac{\rho\phi}{\Delta t}$$

and  $\underline{v}_c$  is calculated from  $\underline{v}_c = -\nabla\phi$ . Thus the procedure for the enforcing of the mass balance consists of the following steps:

- a) Update the momentum equation to  $n'+1$ .

- b) Calculate  $\phi$  from  $\nabla^2 \phi = \nabla \cdot \underline{v}^{n'+1}$ .
- c) Calculate  $\underline{v}_c$  and  $p_c$ .
- d) Update  $\underline{v}^{n+1} = \underline{v}^{n'+1} + \underline{v}_c$  and  $p^{n+1} = p^n + p_c$ .
- e) Repeat this process at the next time step

### *Differencing of the fundamental equations*

The discretization of the momentum balances requires the treatment of the convective terms and the viscous terms. The convective terms are discretized in a fully windward manner using the split coefficient scalar (S.C.S.) form for the incompressible equations. This is handled with the use of conditional velocities which are only nonzero for the proper sign of the velocity. These are calculated in the following manner:

$$v_{\alpha}^{+} = \frac{v_{\alpha} + |v_{\alpha}|}{2}; \quad v_{\alpha}^{-} = \frac{v_{\alpha} - |v_{\alpha}|}{2}$$

where  $\alpha = r, \theta$  or  $\zeta$ .

The time derivative is calculated using 3 point backward (Adams Bashforth) time differencing scheme, which is second order accurate.

$$\frac{\partial v_{\alpha}}{\partial t} \approx \delta_t v_{\alpha} = \frac{3v_{\alpha}^{n'+1} - 4v_{\alpha}^n + v_{\alpha}^{n-1}}{2\Delta t} + O\left(\frac{\Delta t^2}{3} \frac{\partial^3 v_{\alpha}}{\partial t^3}\right)$$

The convective terms are calculated to fourth order accuracy using the three point windward compact (Hermite) differencing. This involves solving a simple tridiagonal matrix for the derivatives at the points  $j-1, j$  and  $j+1$ . The compact forward windward difference for the point  $j$  is given by:

$$\delta_{\Psi}^{+} v_{\alpha} : \frac{\left. \frac{\partial v_{\alpha}}{\partial \Psi} \right|_{j-1}^{+} + 4 \left. \frac{\partial v_{\alpha}}{\partial \Psi} \right|_j^{+} + \left. \frac{\partial v_{\alpha}}{\partial \Psi} \right|_{j+1}^{+}}{6} = \frac{-3v_{\alpha,j} + 4v_{\alpha,j+1} - v_{\alpha,j+2}}{2\Delta \bar{\Psi}} + O\left(\frac{\Delta \bar{\Psi}^4}{20} \frac{\partial^5 v_{\alpha}}{\partial \bar{\Psi}^5}\right)$$

and for the backward difference:

$$\delta_{\Psi}^{-} v_{\alpha} : \frac{\left. \frac{\partial v_{\alpha}}{\partial \Psi} \right|_{j-1}^{-} + 4 \left. \frac{\partial v_{\alpha}}{\partial \Psi} \right|_j^{-} + \left. \frac{\partial v_{\alpha}}{\partial \Psi} \right|_{j+1}^{-}}{6} = \frac{3v_{\alpha,j} - 4v_{\alpha,j-1} + v_{\alpha,j-2}}{2\Delta \bar{\Psi}} + O\left(\frac{\Delta \bar{\Psi}^4}{20} \frac{\partial^5 v_{\alpha}}{\partial \bar{\Psi}^5}\right)$$

The pressure term is calculated to fourth order accuracy using the three point central compact (Hermite) differencing.

$$\bar{\delta}_{\Psi} p : \frac{\left. \frac{\partial p}{\partial \Psi} \right|_{j-1} + 4 \left. \frac{\partial p}{\partial \Psi} \right|_j + \left. \frac{\partial p}{\partial \Psi} \right|_{j+1}}{6} = \frac{p_{j+1} - p_{j-1}}{2\Delta \bar{\Psi}} + O\left(\frac{\Delta \bar{\Psi}^4}{30} \frac{\partial^5 p}{\partial \bar{\Psi}^5}\right)$$

The viscous terms are calculated only to second order accuracy because we are mainly interested in high Reynolds number flows ( $Re \sim 10^4$ ) and thus the numerical error associated with these terms is negligible in the equations compared to the other errors.

$$\delta_{\Psi \Psi} v_{\alpha} = \frac{v_{\alpha,j-1} - 2v_{\alpha,j} + v_{\alpha,j+1}}{\Delta \bar{\Psi}^2} - O\left(\frac{\Delta \bar{\Psi}^2}{12} \frac{\partial^4 v_{\alpha}}{\partial \bar{\Psi}^4}\right)$$

$$\delta_{\Psi} v_{\alpha} = \frac{v_{\alpha,j+1} - v_{\alpha,j-1}}{2\Delta\bar{\Psi}} + O\left(\frac{\Delta\bar{\Psi}^2}{6} \frac{\partial^3 v_{\alpha}}{\partial \bar{\Psi}^3}\right)$$

The finite difference equations for the momentum balances in axial, radial and azimuthal directions can now be established. The discretized radial momentum balance emerges in the form

$$\begin{aligned} \delta_t v_r + \frac{\partial \bar{r}}{\partial r} (v_r^+ \delta_{\bar{r}}^- v_r + v_r^- \delta_{\bar{r}}^+ v_r) + \frac{1}{r} (v_{\theta}^+ \delta_{\theta}^- v_r + v_{\theta}^- \delta_{\theta}^+ v_r) + \frac{\partial \bar{\zeta}}{\partial \zeta} (v_{\zeta}^+ \delta_{\bar{\zeta}}^- v_r + v_{\zeta}^- \delta_{\bar{\zeta}}^+ v_r) - \frac{v_{\theta}^2}{r} = \\ -\frac{1}{\rho} \frac{\partial \bar{r}}{\partial r} \bar{\delta}_r p + \frac{1}{Re} \left\{ \left( \frac{\partial \bar{r}}{\partial r} \right)^2 \delta_{\bar{r}\bar{r}} v_r + \left( \frac{1}{r} \frac{\partial \bar{r}}{\partial r} + \frac{\partial^2 \bar{r}}{\partial r^2} \right) \delta_{\bar{r}} v_r \right. \\ \left. - \frac{v_r}{r^2} + \frac{1}{r^2} \delta_{\theta\theta} v_r + \left( \frac{\partial \bar{\zeta}}{\partial \zeta} \right)^2 \delta_{\bar{\zeta}\bar{\zeta}} v_r + \frac{\partial^2 \bar{\zeta}}{\partial \zeta^2} \delta_{\bar{\zeta}} v_r - \frac{2}{r^2} \delta_{\theta} v_{\theta} \right\} \end{aligned}$$

For the azimuthal momentum balance we get

$$\begin{aligned} \delta_t v_{\theta} + \frac{\partial \bar{r}}{\partial r} (v_r^+ \delta_{\bar{r}}^- v_{\theta} + v_r^- \delta_{\bar{r}}^+ v_{\theta}) + \frac{1}{r} (v_{\theta}^+ \delta_{\theta}^- v_{\theta} + v_{\theta}^- \delta_{\theta}^+ v_{\theta}) + \frac{\partial \bar{\zeta}}{\partial \zeta} (v_{\zeta}^+ \delta_{\bar{\zeta}}^- v_{\theta} + v_{\zeta}^- \delta_{\bar{\zeta}}^+ v_{\theta}) + \frac{v_r v_{\theta}}{r} = \\ -\frac{1}{\rho} \bar{\delta}_{\theta} p + \frac{1}{Re} \left\{ \left( \frac{\partial \bar{r}}{\partial r} \right)^2 \delta_{\bar{r}\bar{r}} v_{\theta} + \left( \frac{1}{r} \frac{\partial \bar{r}}{\partial r} + \frac{\partial^2 \bar{r}}{\partial r^2} \right) \delta_{\bar{r}} v_{\theta} \right. \\ \left. - \frac{v_{\theta}}{r^2} + \frac{1}{r^2} \delta_{\theta\theta} v_{\theta} + \left( \frac{\partial \bar{\zeta}}{\partial \zeta} \right)^2 \delta_{\bar{\zeta}\bar{\zeta}} v_{\theta} + \frac{\partial^2 \bar{\zeta}}{\partial \zeta^2} \delta_{\bar{\zeta}} v_{\theta} + \frac{2}{r^2} \delta_{\theta} v_r \right\} \end{aligned}$$

Finally, the discretized axial momentum balance appears in the form

$$\begin{aligned} \delta_t v_{\zeta} + \frac{\partial \bar{r}}{\partial r} (v_r^+ \delta_{\bar{r}}^- v_{\zeta} + v_r^- \delta_{\bar{r}}^+ v_{\zeta}) + \frac{1}{r} (v_{\theta}^+ \delta_{\theta}^- v_{\zeta} + v_{\theta}^- \delta_{\theta}^+ v_{\zeta}) + \frac{\partial \bar{\zeta}}{\partial \zeta} (v_{\zeta}^+ \delta_{\bar{\zeta}}^- v_{\zeta} + v_{\zeta}^- \delta_{\bar{\zeta}}^+ v_{\zeta}) = \\ -\frac{1}{\rho} \frac{\partial \bar{\zeta}}{\partial \zeta} \bar{\delta}_{\zeta} p + \frac{1}{Re} \left\{ \left( \frac{\partial \bar{r}}{\partial r} \right)^2 \delta_{\bar{r}\bar{r}} v_{\zeta} \right. \\ \left. + \left( \frac{1}{r} \frac{\partial \bar{r}}{\partial r} + \frac{\partial^2 \bar{r}}{\partial r^2} \right) \delta_{\bar{r}} v_{\zeta} + \frac{1}{r^2} \delta_{\theta\theta} v_{\zeta} + \left( \frac{\partial \bar{\zeta}}{\partial \zeta} \right)^2 \delta_{\bar{\zeta}\bar{\zeta}} v_{\zeta} + \frac{\partial^2 \bar{\zeta}}{\partial \zeta^2} \delta_{\bar{\zeta}} v_{\zeta} \right\} \end{aligned}$$

These are the finite difference equations providing the intermediate solution  $\underline{v}^{n'+1}$ .

The divergence of the velocity field is now calculated at the  $n' + 1$  time level and stored in the  $f$  array. It is calculated to fourth order accuracy using five point central derivatives.

$$\begin{aligned} f(r, \theta, \zeta) = \vec{\nabla} \cdot \underline{v}^{n'+1} = \frac{\partial \bar{r}}{\partial r} \left( \frac{v_{r,j-2} - 8v_{r,j-1} + 8v_{r,j+1} - v_{r,j+2}}{12\Delta\bar{r}} \right) + \frac{v_{r,j}}{r_j} \\ + \frac{1}{r} \left( \frac{v_{\theta,k-2} - 8v_{\theta,k-1} + 8v_{\theta,k+1} - v_{\theta,k+2}}{12\Delta\theta} \right) + \frac{\partial \bar{\zeta}}{\partial \zeta} \left( \frac{v_{\zeta,l-2} - 8v_{\zeta,l-1} + 8v_{\zeta,l+1} - v_{\zeta,l+2}}{12\Delta\zeta} \right) \end{aligned}$$

*Algorithm for the pressure equation.*

The Poisson equation for pressure correction is discretized using fourth order accurate central differences. It is solved using the optimized Point Successive Over Relaxation (P.S.O.R) algorithm. Several different techniques were attempted for the solution of this Poisson equation. Besides the P.S.O.R. algorithm, a direct solver in the  $r, \zeta$  plane was used and iteration in the  $\theta$  direction was performed. This proved to be more computationally expensive than the P.S.O.R. algorithm and also required much more memory for the direct solver. Also, the Line Successive over relaxation algorithm was tried. This actually converged the pressure correction solution in fewer iterations but was slower due to the solution of the matrices (tridiagonal for second order accurate and pentadiagonal for fourth order accurate). Also, an ADI technique was tested. This also required more computer time mainly because of the inversion of matrices. Thus the P.S.O.R. algorithm was chosen because of the low memory requirement and computational speed. A computational procedure for determining the optimum acceleration factor  $\omega$  was available. It involves determining the eigenvalues of the Jacobi iteration matrix computationally and then calculating the optimum  $\omega$  for S.O.R. from this.

For the P.S.O.R. algorithm, first the provisional values  $\tilde{\phi}$  are solved for using:

$$\begin{aligned} & \frac{\partial \bar{r}}{\partial r} \left( \frac{-\phi_{j-2}^{i+1} + 16\phi_{j-1}^{i+1} - 30\tilde{\phi}_j + 16\phi_{j+1}^i - \phi_{j+2}^i}{12\Delta\bar{r}^2} \right) \\ & + \left( \frac{1}{r} \frac{\partial \bar{r}}{\partial r} + \frac{\partial^2 \bar{r}}{\partial r^2} \right) \left( \frac{\phi_{j-2}^{i+1} - 8\phi_{j-1}^{i+1} + 8\phi_{j+1}^i - \phi_{j+2}^i}{12\Delta\bar{r}} \right) \\ & + \frac{1}{r} \left( \frac{-\phi_{k-2}^{i+1} + 16\phi_{k-1}^{i+1} - 30\tilde{\phi}_j + 16\phi_{k+1}^i - \phi_{k+2}^i}{12\Delta\theta^2} \right) \\ & + \left( \frac{\partial \bar{\zeta}}{\partial \zeta} \right)^2 \left( \frac{-\phi_{l-2}^{i+1} + 16\phi_{l-1}^{i+1} - 30\tilde{\phi}_j + 16\phi_{l+1}^i - \phi_{l+2}^i}{12\Delta\bar{\zeta}^2} \right) \\ & \frac{\partial^2 \bar{\zeta}}{\partial \zeta^2} \left( \frac{\phi_{l-2}^{i+1} - 8\phi_{l-1}^{i+1} + 8\phi_{l+1}^i - \phi_{l+2}^i}{12\Delta\bar{\zeta}} \right) = f(r, \theta, \zeta) \end{aligned}$$

Then the difference is extrapolated to the new iteration level using

$$\phi^{i+1} = \phi^i + \omega(\tilde{\phi} - \phi^i)$$

This iteration is continued until the maximum change in  $\phi$  at any cell is less than  $10^{-5}$  (i.e.  $Max|\phi^{i+1} - \phi^i| \leq 10^{-5}$ ).

Now, the velocity and pressure corrections are calculated to fourth order accuracy using:

$$\begin{aligned} v_{r,c} &= -\frac{\phi_{j-2} - 8\phi_{j-1} + 8\phi_{j+1} - \phi_{j+2}}{12\Delta\bar{r}} \\ v_{\theta,c} &= -\frac{\phi_{k-2} - 8\phi_{k-1} + 8\phi_{k+1} - \phi_{k+2}}{12\Delta\theta} \\ v_{\zeta,c} &= -\frac{\phi_{l-2} - 8\phi_{l-1} + 8\phi_{l+1} - \phi_{l+2}}{12\Delta\bar{\zeta}} \end{aligned}$$

$$p_c = \frac{3 \rho \phi}{2 \Delta t}$$

and the equations are updated using

$$v_\alpha^{n+1} = v_\alpha^{n'+1} + v_{\alpha,c}; \quad p^{n+1} = p^n + p_c$$

*Boundary and initial conditions.*

The real jet in nature has no boundary conditions since it is in an infinite domain. This could also be simulated by setting the values of all variables to zero at infinity. Therefore the boundary conditions for the computational simulation must not affect the jet and must allow flow structures to pass freely out of the region. The boundary condition which was found to do this well was to set the normal derivative of velocity to zero on the boundaries of the computational region. This can be represented mathematically by

$$\nabla v \cdot \eta = 0$$

where  $\eta$  is the outward pointing normal derivative on the boundary of the computational region. The centerline is not really a boundary condition since information is available on the other side of the centerline. The strategy which worked well was to place the first computational cell at  $\frac{1}{2} \Delta r$  away from the centerline. Then the differences for this cell can be obtained by "reaching over" the centerline. Practically this was obtained by defining rows of cells to the left of the first computational cell and carrying information over into these cells.

The pressure and pressure correction boundary conditions were determined in similar fashion and the same conditions were applied for each. The conditions which were prescribed was to set the pressure gradient in the direction normal to the computational boundary ( $\eta$ ) to zero. This was done on the jet inlet and jet exit planes. On the radial plane parallel to the jet flow, the pressure and the pressure correction were set to zero. This provided stability for the jet and did not affect the solution appreciably. It also increased the rate of convergence of the Poisson equation.

The inlet condition for the jet was obtained using the experimental results of Call and Kennedy (1991). The measured velocity profile at the jet exit was interpolated with a fourth order polynomial. The jet inlet was defined to have no radial or azimuthal velocity ( $v_r = 0, v_\theta = 0$ ) and the axial velocity is given by:

$$v_\zeta = v_{jet} \quad for \quad \frac{r}{r_{jet}} \leq 0.725$$

and

$$v_\zeta = v_{jet} \left( -1.374(10)^2 \left(1 - \frac{r}{r_{jet}}\right)^4 + 1.212(10)^2 \left(1 - \frac{r}{r_{jet}}\right)^3 - 5.225(10)^1 \left(1 - \frac{r}{r_{jet}}\right)^2 + 1.168(10)^1 \left(1 - \frac{r}{r_{jet}}\right)^1 - 2.536(10)^{-3} \left(1 - \frac{r}{r_{jet}}\right)^{-1} \right) \quad for \quad 0.725 \leq \frac{r}{r_{jet}} \leq 1.0$$

The entire flow field was initialized to this profile. The flowfield could have been statically initialized ( $v_r = 0, v_\theta = 0, v_\zeta = 0$ ) and then the inlet profile could be brought in smoothly over a given number of time steps and the flow field could be developed.

An initial startup vortex would travel downstream and leave through the exit section of the computational region. It would establish essentially the same flowfield as the inlet profile. This is the solution to the inviscid problem. This field would then develop the Kelvin Helmholtz instabilities, torroidal vortex structures would emerge, which would later lead to breakdown. This type of initial condition was not chosen since it takes a significant amount of computational time to compute the startup. Also, the analysis of the vortical flow structures developing around the inviscid solution (initialization profile) is very interesting and an important topic. Hence the inviscid solution was taken as initial condition. The pressure was initialized to zero which was found to have no effect on the velocity solution.

Disturbances were introduced at the inlet to initiate the roll-up process. Care must be taken that these disturbances do not violate the continuity equation. For this reason, a disturbance was chosen  $\tilde{v}_\zeta(\theta, t)$  which is only a function of  $\theta$  and time. The disturbance was chosen with known energy spectrum, intensity and frequency. This disturbance form is similar to that used by Rai and Moin (1991). It is given by

$$\tilde{v}_\zeta = \sum_{k=1}^K \sum_{n=1}^N A_{l,n} \sin(k\theta + \phi_\theta) \sin\left(\frac{2\pi n t}{\tau} + \phi_t\right)$$

where

$$A_{l,n} = c v_{jet} r_{jet} \delta^{k-1} \gamma^{n-1}, \quad \delta = 0.25, \quad \gamma = 0.5, \quad c = 0.1$$

In the above disturbance, two modes in both  $\theta$  and time were chosen (i.e.  $K = 2, N = 2$ ).

#### *Time step restriction*

The time step is calculated using the maximum stable explicit time step for the model problem. Since the high Reynolds number jet is mostly convection dominated, the convective terms dominate the time step limitation. The extension to three dimensions considers stability in all three dimensions and essentially adds the Courant numbers in each direction to get an effective Courant number. An extensive analysis for the Adams Bashforth time differencing and the fourth order accurate compact three point backward windward differencing on the convective terms revealed that the maximum stable Courant number is  $(\frac{1}{2})$ . For the viscous terms, the maximum stable diffusion number is  $(\frac{1}{6})$ . Thus, we have the maximum stable time step computed as:

$$\Delta t|_{max} = \frac{\frac{1}{2}}{\frac{\partial \bar{r}}{\partial r} \frac{|v_r|}{\Delta \bar{r}} + \frac{1}{r} \frac{|v_\theta|}{\Delta \theta} + \frac{\partial \bar{\zeta}}{\partial \zeta} \frac{|v_\zeta|}{\Delta \bar{\zeta}} + \frac{1}{3Re} \left( \left( \frac{\partial \bar{r}}{\partial r} \right)^2 \frac{1}{\Delta \bar{r}^2} + \frac{1}{r^2 \Delta \theta^2} + \left( \frac{\partial \bar{\zeta}}{\partial \zeta} \right)^2 \frac{1}{\Delta \bar{\zeta}^2} \right)} \Big|_{min}$$

This is computed automatically during the solution procedure and the maximum stable time step (with a safety factor) is used for updating the momentum equations.

#### *Code verification*

Extensive tests were carried out to ensure that the solution method produces the correct solution. First the laminar jet solution of Schlichting (1960) was calculated for the plane and the axisymmetric case. Excellent agreement with the analytical solution was achieved. The second test was the comparison of the spreading rate for the unsteady turbulent

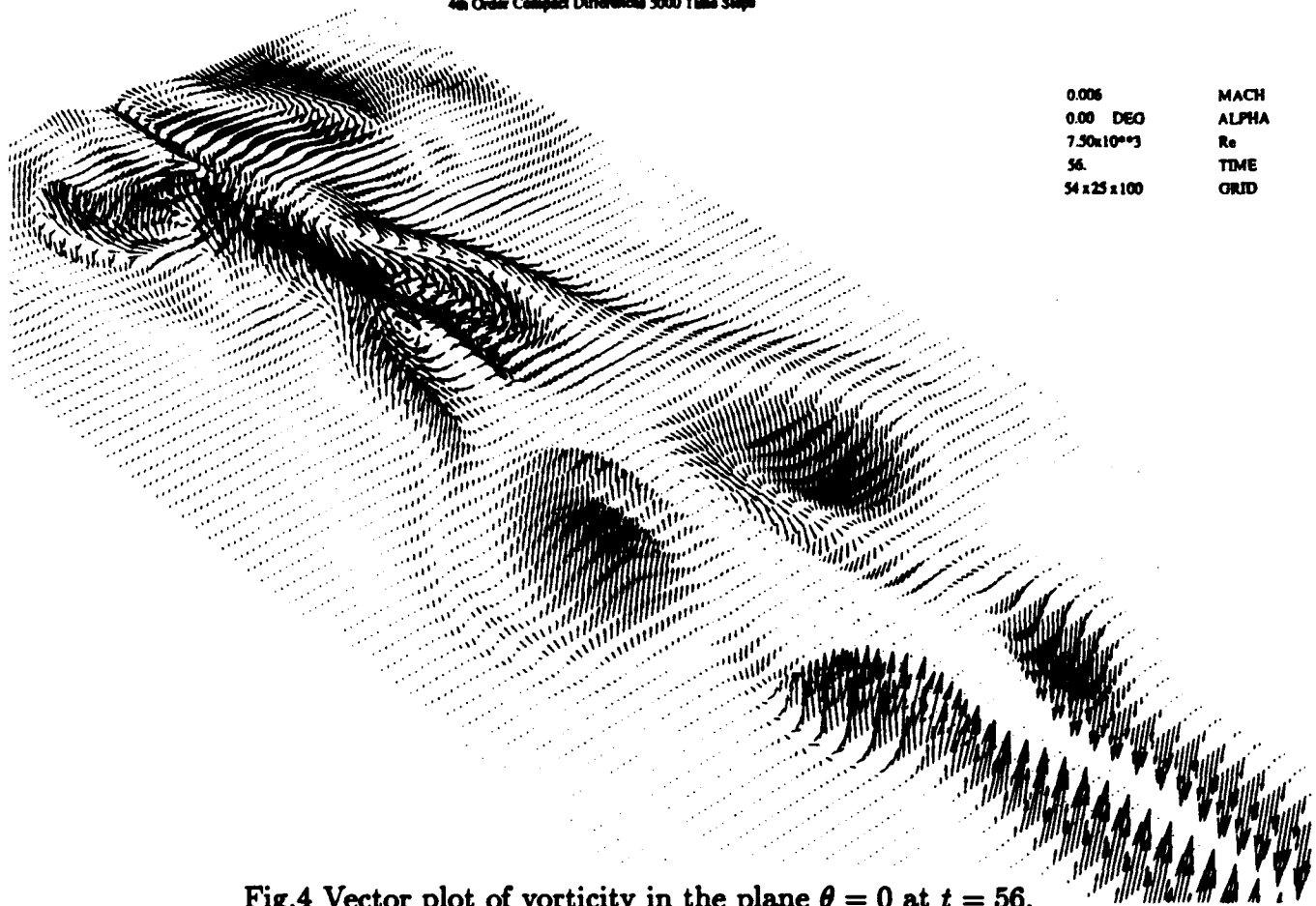
solution with the experimental values which was within the experimental error. Finally, the results of linear stability theory (Michalke and Herrmann, 1982) were verified with the three dimensional version of the code.

### *Results and discussion.*

The turbulent flow in a round jet was simulated with a standard second accurate method and the fourth order accurate finite-difference methods discussed in the previous sections. The simulation must be regarded as Large Eddy Simulation since the grid is not able to resolve all scales of the flow. Monotonic schemes can be viewed as LES methods where the discretization error plays the role of a numerical filter (Boris, 1989). The Reynolds number is defined by  $Re \equiv \frac{u_0 D}{\nu} = 15000$ , where  $u_0$  denotes the bulk exit velocity and  $D$  the jet pipe diameter. The grid was set up as  $54 \times 25 \times 100$  for the radial, azimuthal and longitudinal directions and stretching transformations were applied to concentrate the grid in the high shear region. The computational domain covered the first ten diameters of the jet. Disturbances were introduced at the jet pipe exit to induce the roll-up of the vortex layer and the subsequent break up of the ring structures. All calculations were carried out on workstations.

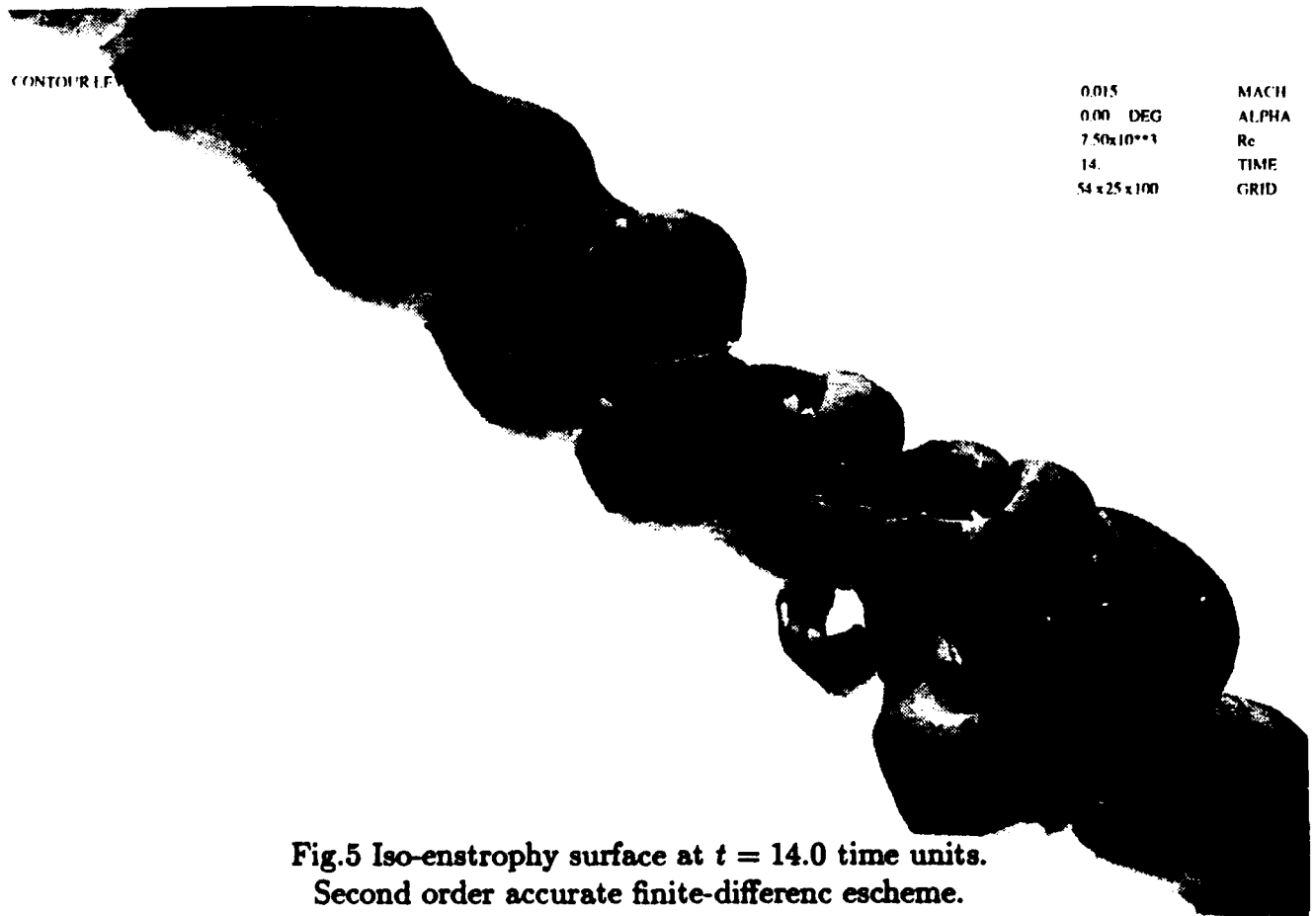
Preliminary results for the second and fourth order methods are presented in Fig.4 to Fig.13. The instantaneous vorticity vectors in Fig.4 are plotted in the plane  $\theta = 0$  for the fourth order method at the dimensionless time  $t = 56$ . Vorticity is concentrated in the shear layer as the fluid leaves the jet pipe. The shear layer starts to roll up leading to amplification of vorticity and a big ring vortex is formed at about four diameters downstream. This large structure breaks up as it moves downstream generating fluctuations of smaller scale. The axial range shown corresponds to about eight jet pipe diameters and close to fully developed flow. The early stage in the development of this large structure is illustrated as iso-surface for enstrophy in Fig.5 and Fig.6. At dimensionless time  $t = 14.0$  in these two figures the formation of braided structures can be observed (note that the flow direction is from the lower right corner to the upper left corner) breaking the azimuthal symmetry of the flow. The large ring vortex is not yet fully established but can be seen at the later time  $t = 54$  in Fig.7 and at  $t = 55$  in Fig.8. The growth of the dominant ring peaks at about  $t = 54$  with the next upstream vortex just in the beginning of formation. The next Fig.8 shows the formation of the upstream vortex well under way as the large ring moves downstream. The break up of the downstream vortex nearly completed at  $t = 55$ . A different illustration of the vortex break up is shown in Fig.9 (second order accurate scheme) as vortex lines (tangential to vorticity). It is evident that the break up process involves the production of axial and azimuthal vorticity components.

The dynamics of particles released near the center of the jet pipe is shown in Fig.10 to Fig.13. The pathlines of several (hexadecane) particles show that they move through the potential core without radial dispersion and undergo violent motion in radial direction as the large vortex structure at about five diameters is encountered. The dispersion of fluid material points (massless particles) is shown in Fig.11 as a function of the time of flight. The scatter plots for fluid material points in Fig.12 and hexadecane particles in Fig.13 prove that fluid material points undergo more radial dispersion than the heavy particles.



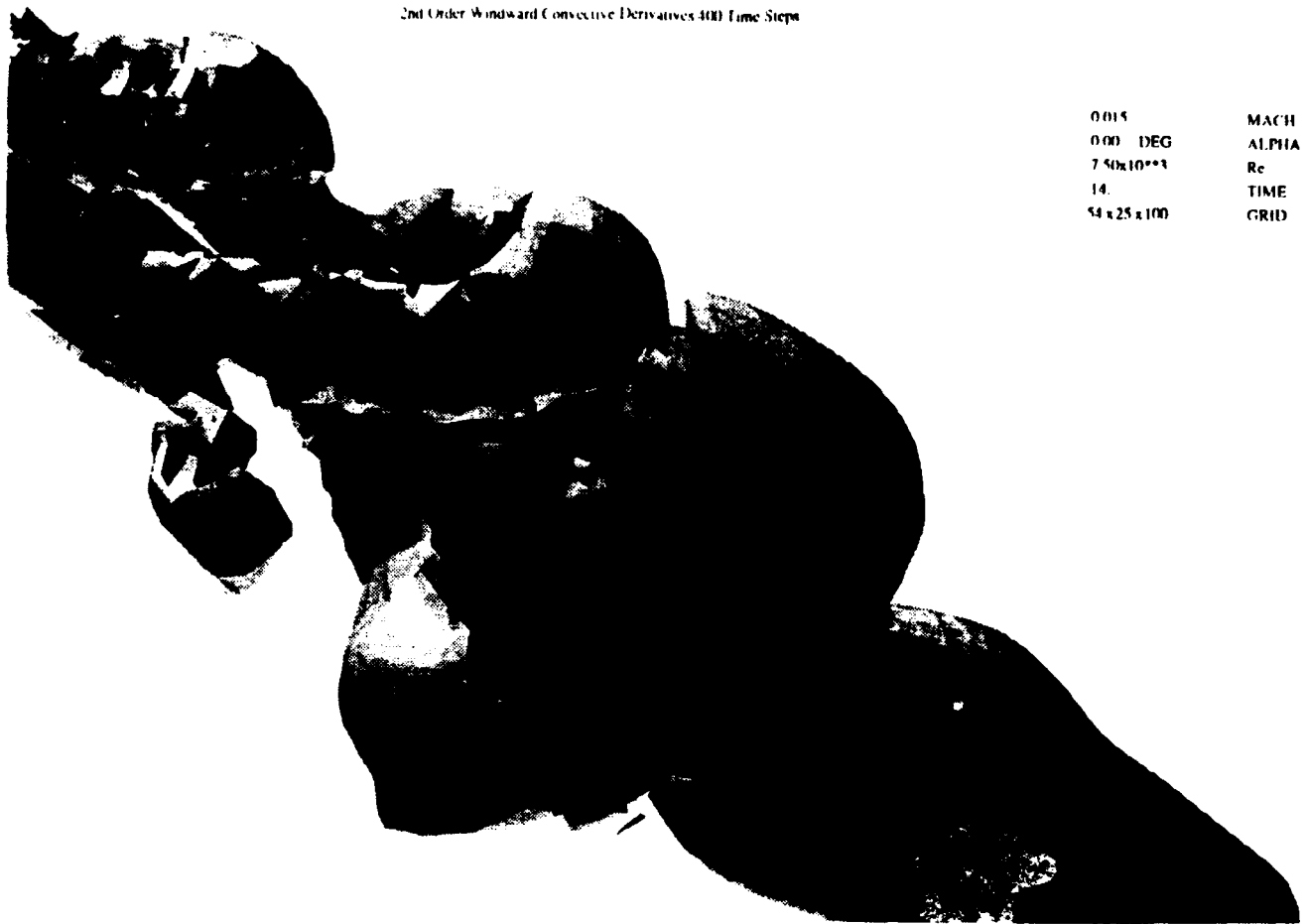
0.006	MACH
0.00 DEG	ALPHA
$7.50 \times 10^{**3}$	Re
56.	TIME
54 x 25 x 100	GRID

Fig.4 Vector plot of vorticity in the plane  $\theta = 0$  at  $t = 56$ .  
Fourth order accurate finite-difference scheme.



0.015	MACH
0.00 DEG	ALPHA
$7.50 \times 10^{**3}$	Re
14.	TIME
54 x 25 x 100	GRID

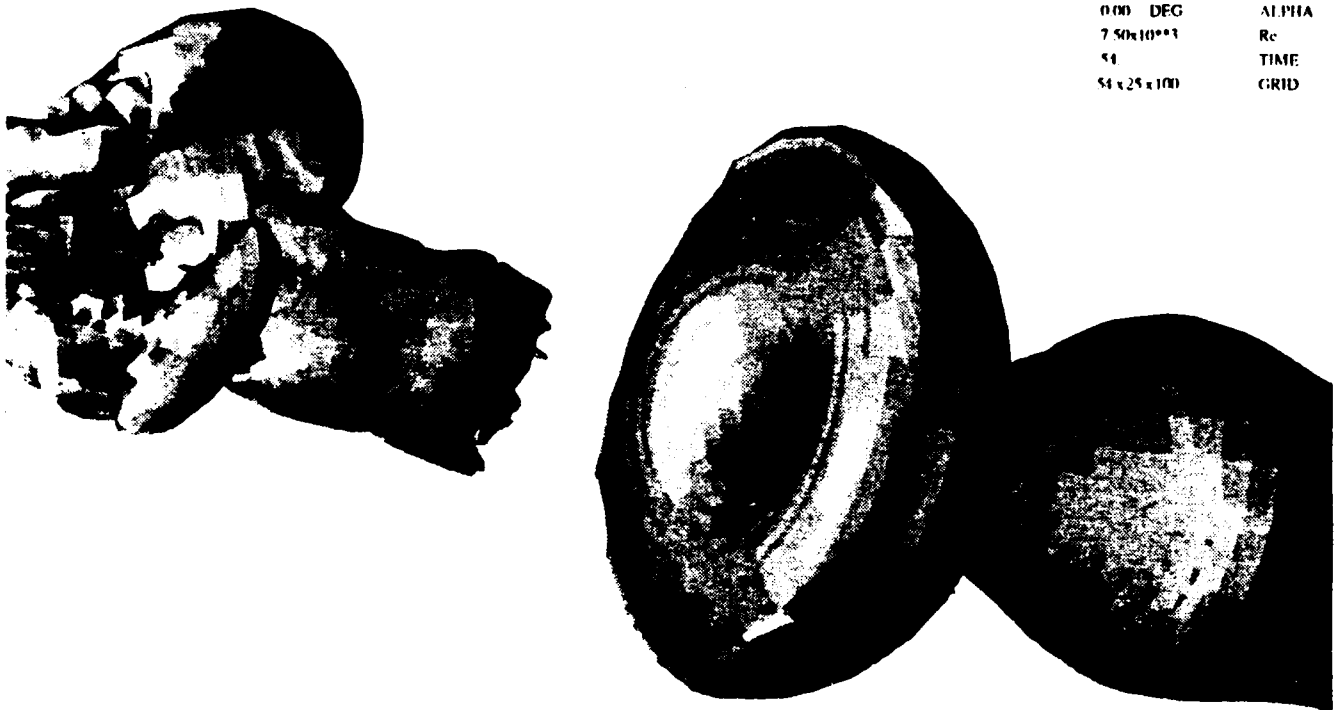
Fig.5 Iso-entropy surface at  $t = 14.0$  time units.  
Second order accurate finite-difference scheme.



0.015	MACH
0.00 DEG	ALPHA
$7.50 \times 10^{**3}$	Re
14.	TIME
$54 \times 25 \times 100$	GRID

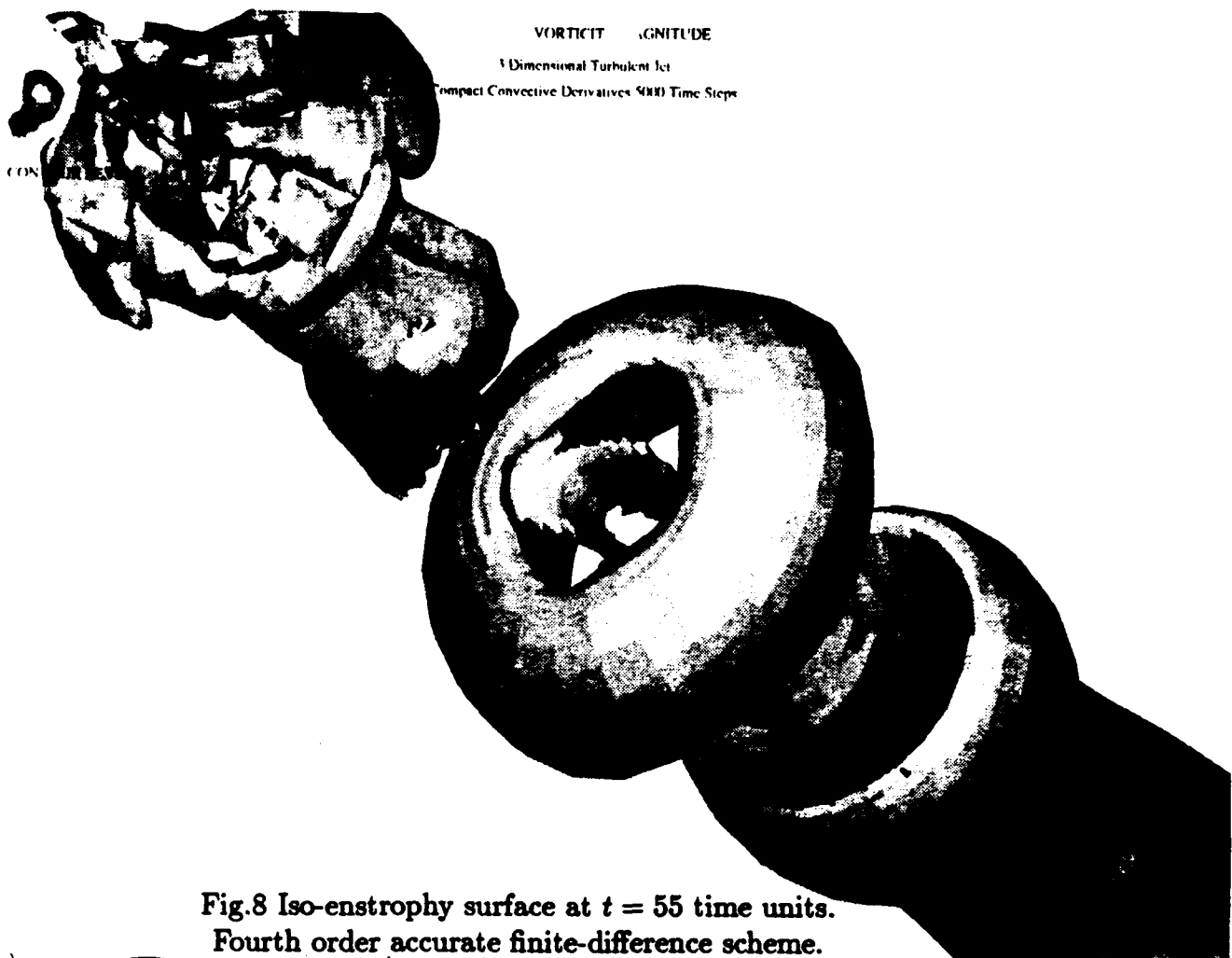
Fig.6 Close-up of the iso-entropy surface in Fig.5

CONTOUR LEVELS



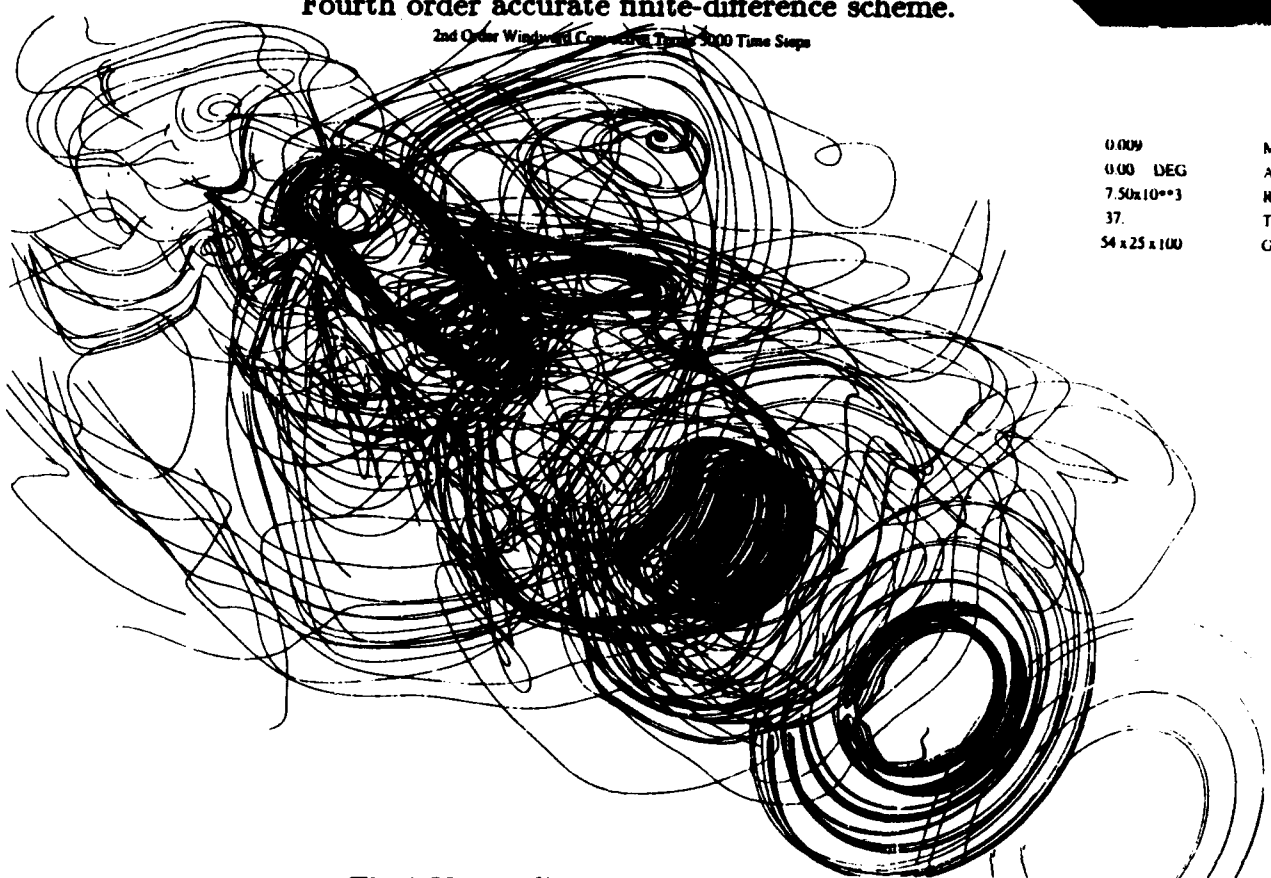
0.006	MACH
0.00 DEG	ALPHA
$7.50 \times 10^{**3}$	Re
54	TIME
$54 \times 25 \times 100$	GRID

Fig.7 Iso-entropy surface at  $t = 54$  time units.  
Fourth order accurate finite-difference scheme.



VORTICITY MAGNITUDE  
3 Dimensional Turbulent Jet  
Compact Convective Derivatives 4000 Time Steps

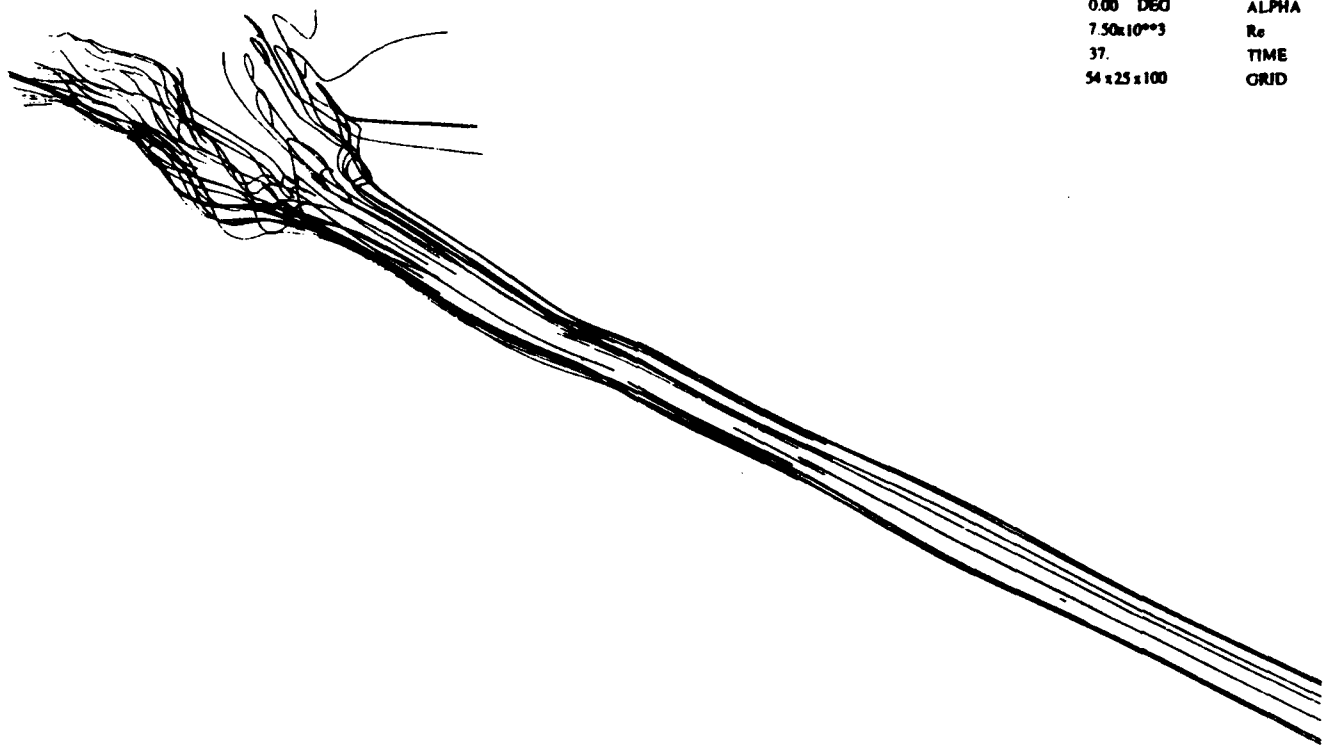
**Fig.8 Iso-entropy surface at  $t = 55$  time units.  
Fourth order accurate finite-difference scheme.**



2nd Order Windward Compaction 3000 Time Steps

0.009	MAC
0.00 DEG	ALP
$7.50 \times 10^{**3}$	Re
37.	TIM
54 x 25 x 100	GRID

**Fig.9 Vortex lines at  $t = 37$  time units.  
Second order accurate finite-difference scheme.**



0.009	MACH
0.00	ALPHA
$7.50 \times 10^{**3}$	Re
37.	TIME
$54 \times 25 \times 100$	GRID

Fig.10 Pathlines for hexadecane particle released near the jet pipe axis at  $t = 37$  for the second order accurate scheme

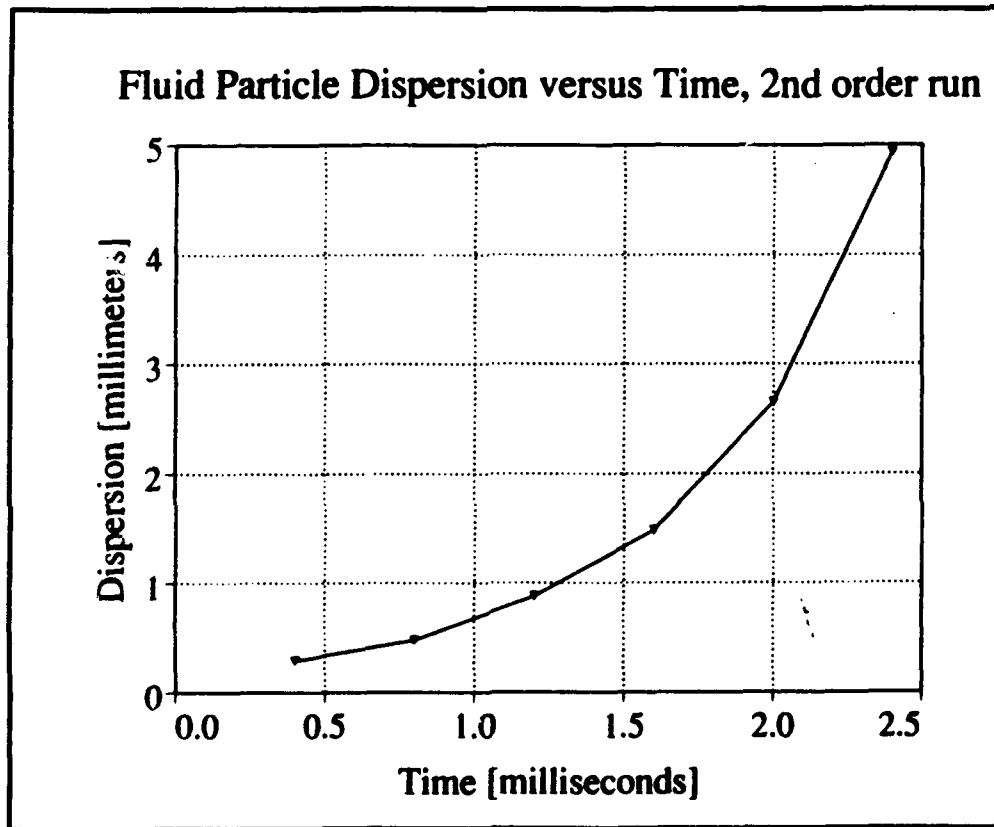
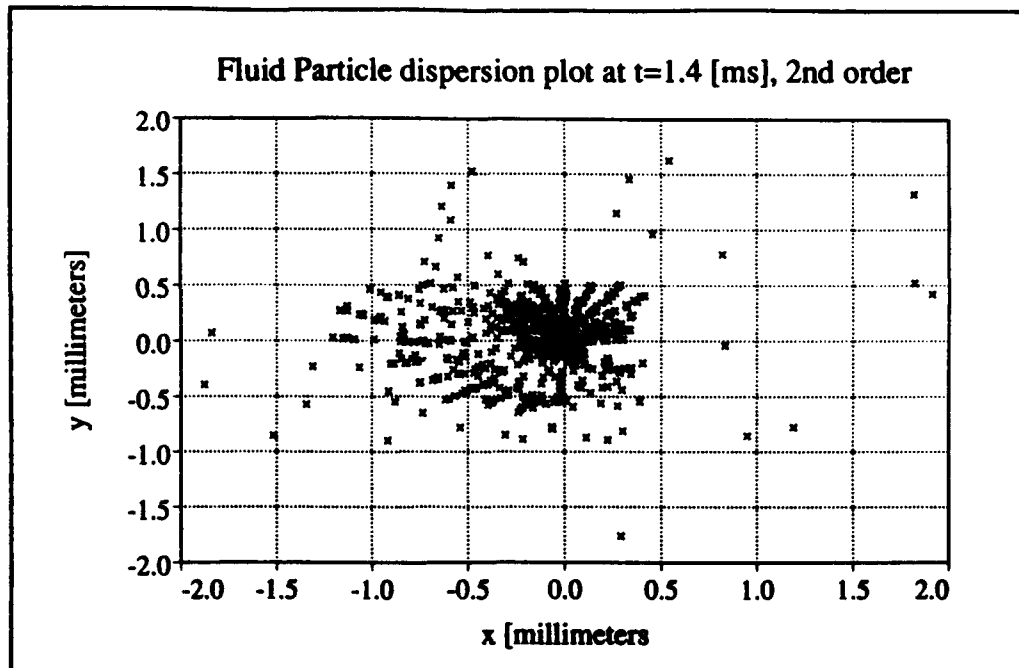
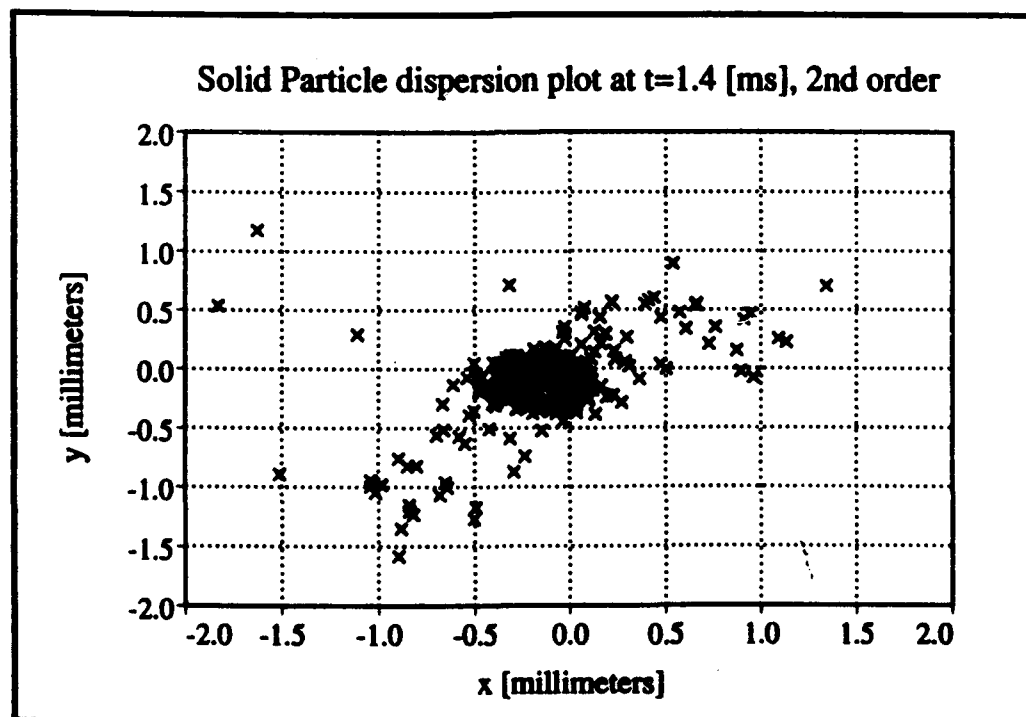


Fig.11 Fluid particle dispersion as function of the time of flight.



**Fig.12** Scatter plot of fluid material points at  $t = 1.4$  ms.



**Fig.13** Scatter plot of hexadecane particles at  $t = 1.4$  ms.

### 1.3 References.

Anderson, C. and Greengard, C. (1984), "On vortex methods", *SIAM J. Numerical Analysis* **22**, 413

Antonia, R.A., Satyaprakash, B.R. and Hussain, A.K.M.F. (1980), "Measurements of dissipation rate and some other characteristics of turbulent plane and circular jets", *Phys. Fluids* **23**, 695

Ashurst, W.T. and Meiburg, E. (1988), "Three-dimensional shear layers via vortex dynamics", *J. Fluid Mechanics* **189**, 87

Boris, J.P. (1990), "Comments on subgrid turbulence models and large eddy simulations", in *Whither Turbulence? or Turbulence at the Crossroads* (J.L. Lumley ed.), *Lecture Notes in Physics* vol. 357, Springer V., 344

Call, C.J. and Kennedy, I.M. (1991), "A technique for measuring Lagrangian and Eulerian particle statistics in a turbulent flow", *Exper. in Fluids* **12**, 125.

Chorin, A.J. (1980), "Vortex models and boundary layer instability", *SIAM J. Sci. Stat. Comput.* **1**, 1

Crow, S.C. and Champagne, F.H. (1971), "Orderly structure in jet turbulence", *J. Fluid Mechanics* **48**, 547

Dibble, R. W., Kollmann, W., Farshchi, M. and Schefer, R. W. (1986), "Second Order Closure for Turbulent Nonpremixed Flames: Scalar Dissipation and Heat Release Effects", *21st Symp. (Int.) Comb., The Comb. Inst.*, 1329

Faeth, G.M. (1983), "Evaporation and combustion of sprays", *Progr. Energy Comb. Sci.* **9**, 1

Hansell, D., Kennedy, I.M. and Kollmann, W. (1992), "A simulation of particle dispersion in a turbulent jet" to appear in *J. Multi-Phase Flow*.

Leonard, A. (1985), "Computing three-dimensional incompressible flows with vortex elements", *Ann. Rev. Fluid Mech.* **17**, 523

Lundgren, T.S. and Ashurst, W.T. (1989), "Area-varying waves on curved vortex tubes with application to vortex breakdown", *J. Fluid Mechanics* **200**, 283

Michalke, A. and Herrmann, G. (1982), "On the inviscid instability of a circular jet with external flow", *J. Fluid Mechanics* **114**, 343

Moore, D.W. (1972), "Finite amplitude waves on aircraft trailing vortices", *Aeronaut. Quart.* **23**, 307

Odar, F. and Hamilton, W.S. (1964), "Forces on a sphere accelerating in a viscous fluid", *J. Fluid Mech.* **18**, 302

Putnam, A. (1961), "Integrable form of droplet drag coefficient", *ARS J.* **31**, 1467.

- Rai, M.M. and Moin, P. (1991), "Direct simulations of turbulent flow using finite-difference schemes", *J. Comput. Physics* **96**, 15
- Renksizbulut, M. and Yuen, M.C. (1983), "Experimental study of droplet evaporation in a high-temperature air stream", *J. Heat Transfer* **105**, 384
- Schlichting, H. (1960), "Boundary layer theory", 4th edition, McGraw Hill.
- Shuen, J.S., Solomon, A.S.P., Zhang, Q.F. and Faeth, G.M. (1985), "Structure of particle laden jets: Measurements and predictions", *AIAA J.* **23**, 396
- Snyder, W.K. and Lumley, J.L. (1971), "Some measurements of particle velocity autocorrelation functions in a turbulent flow", *J. Fluid Mech.* **48**, 41
- Solomon, A.S.P., Shuen, J.S., Zhang, Q.F. and Faeth, G.M. (1985), "Structure of non-evaporating sprays, part I: Initial conditions and mean properties", *AIAA J.* **23**, 1548
- Solomon, A.S.P., Shuen, J.S., Zhang, Q.F. and Faeth, G.M. (1985), "Structure of non-evaporating sprays, part II: Drop and turbulence properties", *AIAA J.* **23**, 1724
- Yule, A.J. (1978), "Large-scale structure in the mixing layer of a round jet", *J. Fluid Mechanics* **89**, 413
- Yuu, S., Yasukouchi, N., Hirosawa, Y. and Jotaki, T. (1978), "Particle turbulent diffusion in a dust laden round jet", *AIChE J.*, **24**, 509

## **2.0 Personnel.**

I. M. Kennedy	P. I.	15% time
W. Kollmann	Co - P. I.	10% time
C. J. Call	Ph. D. candidate	50% time
J. J. Lienau	Ph. D. candidate	25% time

## **3.0 Publications.**

Call, C.J. and Kennedy, I.M. (1991), "Particle dispersion in a turbulent shear flow", AIAA Paper 90-0468, AIAA Aerospace Sciences Meeting, Reno NV.

Call, C.J. and Kennedy, I.M. (1991), "A technique for measuring Lagrangian and Eulerian particle statistics in a turbulent flow", *Exper. in Fluids* **12**, 125.

Call, C.J. and Kennedy, I.M. (1991), "Particle dispersion and velocity statistics in a turbulent shear flow: Measurements and simulations", Paper No. 91-38 Spring Meeting of the Western States Section of the Combustion Institute, Boulder CO, March 1991.

Call, C.J. and Kennedy, I.M. (1992), "Droplet dispersion, velocity and vaporisation in heated and unheated jets", Paper No. 92-42 Spring Meeting of the Western States Section of the Combustion Institute, Corvallis OR, March 1992.

Hansell, D., Kennedy, I.M. and Kollmann, W. (1992), "A simulation of particle dispersion in a turbulent jet", accepted for publication in *J. Multi-Phase Flow*.

## **4.0 Presentations.**

Papers based on work for this project have been delivered in the following venues:

### **1989:**

- (1) Western States Section Meeting of the Combustion Institute, Livermore, CA, October 1989.
- (2) 10th Australasian Fluid Mechanics Conference, Melbourne, Dec. 1989.

### **1990:**

- (1) AIAA Aerospace Sciences Meeting, Reno NV, Jan. 1990.
- (2) Poster presentation at the 23rd Int. Combustion Symposium, Orleans, France 1990.

### **1992:**

- (1) Western States Section Meeting of the Combustion Institute, Corvallis, OR, March 1992.

## **5.0 Interactions.**

This work has been presented at the Spring Meetings of the Western States Section of the Combustion Institute.

Collaboration has been initiated with Allison Gas Turbines to implement a model of soot processes in flames. This work is in conjunction with a student of Prof. R. Santoro. In addition, Dr. Nader Rizk, who is engaged in spray modelling at Allison, has expressed an interest in using the results of this project in validation of his stochastic simulations. This interaction was established in 1991 during a visit by the P.I. to Allison in Indianapolis.

**Inventions.**

There were no inventions.

**Appendix:**

Call, C.J. and Kennedy, I.M. (1991), "A technique for measuring Lagrangian and Eulerian particle statistics in a turbulent flow", *Exper. in Fluids* **12**,125.

# A technique for measuring Lagrangian and Eulerian particle statistics in a turbulent flow

C. J. Call and I. M. Kennedy

Dept. of Mechanical, Aeronautical, and Materials Engineering, University of California, Davis, CA 95616, USA

**Abstract.** An experimental technique is described which has been developed to study particle dispersion in a round turbulent jet. Droplets are injected on the jet axis, and a laser sheet and position sensitive photomultiplier tube are used to track their radial displacement. Data processing is greatly simplified compared to video or photo imaging techniques which provide similar measurements. Statistically large samples are used to calculate dispersion and axial velocity as a function of axial downstream distance or particle time-of-flight. Dispersion and velocity statistics can be computed which are Lagrangian or Eulerian in nature. The technique has been demonstrated with 69  $\mu\text{m}$  droplets of hexadecane in a jet of air with a Reynolds number of 15,000; in principle it could be used to study the motion of very small, quasi-fluid particles.

## 1 Introduction

Many practical industrial processes require the rapid mixing of liquid or solid particles within a gaseous phase. Particle-turbulence interaction plays a fundamental role in the mixing of these phases. Examples include spray and pulverized coal combustion. Both gas phase turbulence and particle response characteristics determine the mixing rate.

This paper reports a novel experimental technique developed to measure particle displacement and velocity. The measurements can yield either Lagrangian or Eulerian statistics of dispersion and velocity; single particles are tracked from a known initial point, and the time-of-flight is known for each particle. Most measurements of dispersion presented in the literature are of the purely Eulerian type; a probe or other observation apparatus rests at a fixed location and collects a sample of particles which find their way to the probe volume. Examples of this methodology are the measurements of Yuu et al. (1978) and Hardalupas et al. (1989), whereby an entire flow was seeded while measurements were obtained at fixed downstream points.

Lagrangian measurements of particle statistics are particularly useful. The most common spray modelling approaches involve integrating a particle path through a flow-field. This approach uses a Lagrangian description of particle motion for each droplet and spray statistics are computed

from a large sample of single particle integrations. Information about the assumptions and models that are incorporated into these calculations can be inferred only from Eulerian statistics at present.

There are three notable studies in which Lagrangian measurements of dispersion are presented. Snyder and Lumley (1971) photographed particles transported in a grid generated flow. Transformations were used to compensate for turbulence decay so that the fluctuations were stationary with respect to the transformed variables. Direct measurements of the particle velocity correlation and the dispersion rate were presented. A primary drawback of the technique was the time expense associated with obtaining and analyzing photographs and the restricted number of samples that were obtained. A similar technique is under development by Lee et al. (1989); it is capable of providing dispersion measurements for droplets in isothermal pipe turbulence. An automated photograph analysis is used. Another technique has been utilized recently by Vames and Hanratty (1989) to obtain Lagrangian measurements of water droplet dispersion in pipe generated turbulence. The approach is similar to that used by Wel. and Stock (1983). A potential drawback to this technique is that the time-of-flight for each droplet is not measured. Instead an average time-of-flight is determined from the integration of mean velocity data. This point will be discussed further in the results.

## 2 Theoretical foundation

The basic theory for the dispersion of a particle, developed by Taylor (1921), considers the displacements of a fluid particle in a stationary, isotropic flow. The fundamental result of the analysis is the following expression for the particle dispersion as a function of the velocity correlation:

$$\sigma_x^2(t) = 2 \int_0^t \int_0^{t'} \langle v_x(t') v_x(t'') \rangle dt'' dt' = 2 \langle v_x^2 \rangle \int_0^t \int_0^{t'} R^L(t', t'') dt'' dt' \quad (1)$$

where  $v_x$  is the particle velocity relative to the mean flow.  $R^L(t', t'')$  is the particle Lagrangian velocity autocorrelation

function defined by  $\langle v_x(t') v_x(t'') \rangle / \langle v_x^2 \rangle$ . The dispersion  $\sigma_x^2$  is the mean square particle displacement along the  $x$ -axis. Displacement is a random variable, and averages refer to ensembles of realizations of the variable. The statistically averaged particle velocity,  $\langle v_x^2 \rangle^{1/2}$ , is constant in time for stationary flows. Direct use of the theory in real flows requires knowledge of  $R^L$ , which is generally unknown.

Two important special cases of Taylor's original theory are observed. For short separation times, the particle velocity is perfectly correlated with itself: as  $t'' - t' \rightarrow 0$  then  $R^L(t', t'') \rightarrow 1$ . Equation (1) can be integrated, and the dispersion is quadratic in time. For large times, the particle velocity becomes uncorrelated,  $R^L(t', t'') \rightarrow 0$ , and the dispersion is linear in time. The slope of this line is defined to be the particle diffusivity.

The above results for a fluid particle can be generalized to three dimensions and under restricted conditions the theory can be extended to nonhomogeneous self-preserving flows. The linear behavior of Taylor's theory for large times should also be observed in the dispersion of fluid particles in a round jet as shown by Batchelor (1957). Taylor's original presentation was developed for the dispersion of a fluid particle, but can be applied to larger particles with the appropriate definition of  $R^L$  based on the velocity correlation of the discrete particle. A limited theory has been developed for the dispersion of a discrete particle in homogenous turbulence by Friedlander (1957), Saffman (1960) and Reeks (1977).

### 3 Experimental technique

A schematic of the experiment is shown in Figure 1. A steady stream of monodisperse droplets are generated using a piezoelectric transducer. The droplets are accelerated by the air flow in the nozzle contraction. As each droplet passes from the nozzle, it intercepts a He-Ne laser beam which is monitored by a photo-diode. The diode signal is used as a trigger for the data acquisition system and allows the time-of-flight to be measured for each droplet. As the droplet travels axially downstream, it is radially displaced by the jet turbulence and the displacement from the jet axis is measured. The experimental difficulty in tracking individual particles from a known initial point has been overcome using a sheet of laser light and a position-sensitive photomultiplier tube (pmt). Droplet dispersion statistics are computed from the position measurements. For the present study the jet Reynolds number is 15,000 based on a nozzle diameter of 7 mm. The droplet diameter is measured by video microphotography, with an estimated uncertainty of  $\pm 2 \mu\text{m}$ . The droplet size is governed by a nozzle attached to the transducer. The present data are for 69  $\mu\text{m}$  hexadecane droplets.

The droplet generation frequency is nominally 10 Hz. The total data collection and computer processing time is approximately 2 minutes per 1000 droplets. The droplets are separated by more than 1000 droplet diameters; hence, the droplets are non-interacting and have a negligible effect on

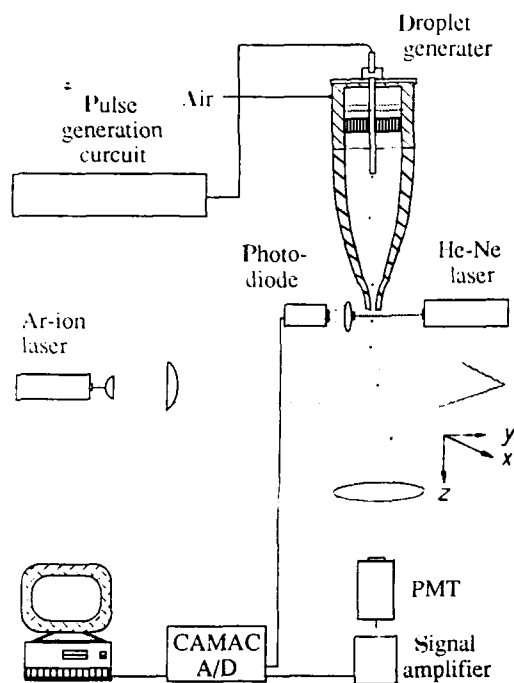


Fig. 1. Sketch of experimental apparatus

the gas phase flow properties. The vaporization of hexadecane droplets is negligible over the times of flight under investigation (typically less than 50  $\mu\text{s}$ ).

A 514 nm Argon ion laser beam, rated at 4 W, is used to form a nominally 100 mm wide laser sheet using two cylindrical lenses. Light scattered from the droplets is focused to a spot on a Hamamatsu position sensitive photomultiplier tube. The pmt has four diametrically opposed outputs and an effective active area of 1600  $\text{mm}^2$ . The photocurrent signals are amplified, low-pass filtered and fed to a four channel analog to digital converter, which samples each pulse simultaneously at 20 kHz. The instantaneous position of the droplet can be determined by comparing the four signals along each pulse.

Figure 2 shows a typical signal from opposite sides of the anode as a droplet passes through the laser sheet. The base line or  $dc$  offset on both signals ( $V_{0,1}$ ,  $V_{0,2}$ ) is due to the background Rayleigh scattering from the air and stray laser reflections. This scattering cannot be eliminated optically and hence is subtracted during data processing. The ratio of the difference of the two signals to the sum of the signals yields a unitless function  $X$  which is proportional to the  $x$  displacement from the centerline:

$$X = \frac{(V_2 - V_{0,2}) - (V_1 - V_{0,1})}{(V_2 - V_{0,2}) + (V_1 - V_{0,1})} z, X \quad (2)$$

Calibration is then necessary to relate  $X$  to the actual distance of the droplet along the  $x$ -axis. The system has been calibrated using droplets in a laminar flow at known positions and the calibration is shown in Fig. 3. It is apparent

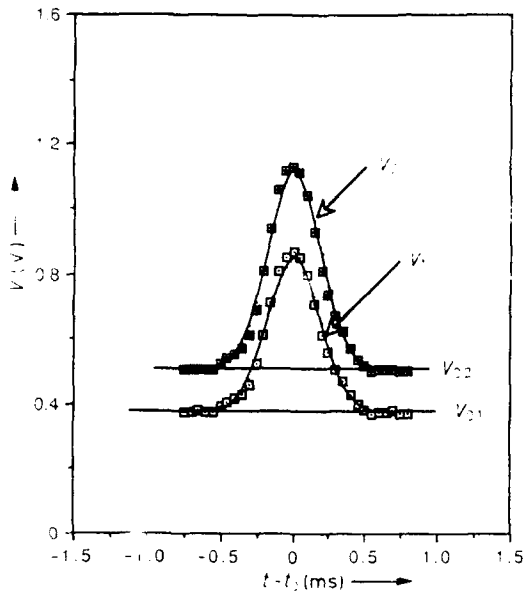


Fig. 2. Typical signals from opposing sides of the anode as a droplet passes through the laser sheet

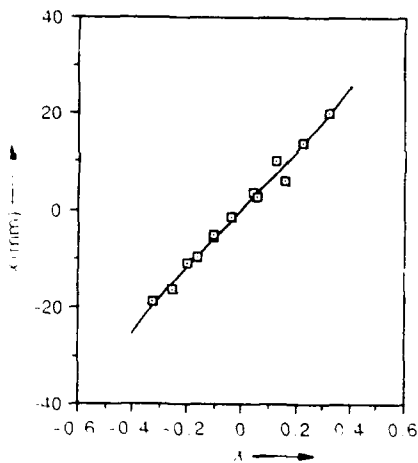


Fig. 3. Calibration data for position measurements. Solid line is a third order curve fit

that the pmt response is quite linear in position over a wide range. In order to cope with outlying droplets we have chosen to fit the calibration measurements with a 3<sup>rd</sup> order polynomial. Because the collection optics and pmt are located on the jet axis  $z$ , the calibration in the  $y$  direction is identical to that in the  $x$ . (Fig. 1 illustrates the orientation of the coordinate axes.)

Axial droplet velocities are measured by timing the passage of droplets through the laser sheet. A typical total pmt signal is shown in Fig. 4, obtained by summing the four channels. The signal is approximated well by a Gaussian function as would be expected from an Argon ion laser beam. The width of the pulse is proportional to the variance of the Gaussian curve fit,  $\sigma$ . This parameter is related, in turn, to the transit time of the droplets as it pass through the

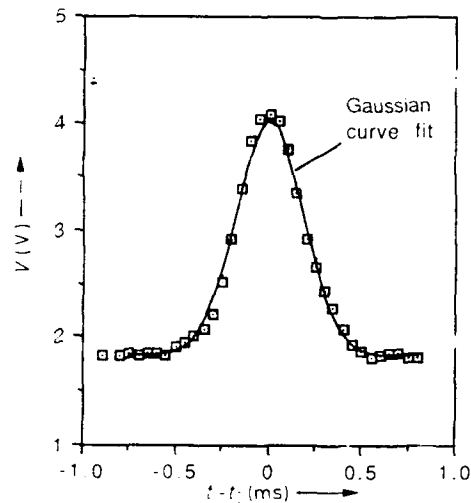


Fig. 4. Typical total pmt signal, obtained by summing all four channels

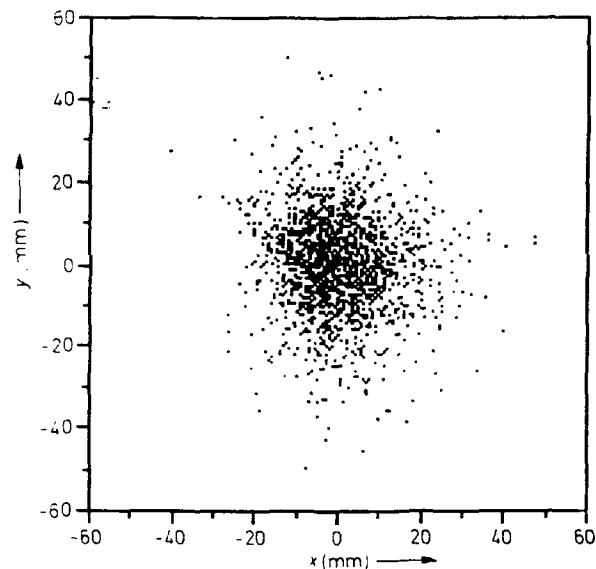


Fig. 5. Scatter plot for 69  $\mu\text{m}$  hexadecane droplets at  $z/D = 51$

laser beam. Assuming the velocity gradients in the axial direction are not large, this time is inversely proportional to the droplet velocity. Calibration of velocity is performed using two closely spaced laser sheets with a known separation distance.

### 3.1 Analysis of particle position

As each droplet passes through the sheet a series of  $x, y$  pairs are obtained, each pair separated in time by 50  $\mu\text{s}$  (due to the 20 kHz digitization rate). These pairs are then averaged, providing a mean displacement for each drop. A distribution of droplet displacements is shown in Fig. 5. The scatter data are typical for an axial location of  $z/D = 51$ . The pdfs for displacement of the droplets in the  $x$  or  $y$  direction are

Gaussian to within the accuracy of the experimental data. There is no a priori reason to expect a Gaussian distribution since the droplet trajectories are through a non-homogeneous flow field which is non-stationary in the Lagrangian reference frame. However, the result is not surprising since Gaussian distributions have also been observed for particle displacement in pipe generated turbulence.

One experimental objective is to measure the dependence of dispersion on axial position and on droplet time-of-flight. From these measurements, a particle diffusivity and root mean square (rms) radial velocity can be estimated by considering a limiting case of Taylor's theory. The diffusivity is dependent on the flow characteristics and time scales, as well as particle parameters.

The radial dispersion  $\sigma_r^2$  is computed using the following expression:

$$\sigma_r^2 = \frac{1}{n} \sum_{i=1}^n (x_i^2 + y_i^2) \quad (3)$$

where  $n$  is the number of droplet samples obtained and the  $x_i$  and  $y_i$  are the measured displacements from the jet axis for each droplet. The dispersion in the  $x$  or  $y$  direction is also readily computed and since the flow field and dispersion are axisymmetric,  $\sigma_x^2 = \sigma_y^2$ . For experimental dispersion measurements, a total of 1000 droplets are used for statistics at each axial location downstream from the air jet nozzle. The time-of-flight and radial displacement are recorded for each droplet at a particular axial location.

### 3.2 Analysis of particle velocity

The axial velocities of the droplets have been measured at a number of axial stations along the jet. Figure 6 presents two velocity probability density functions at 27 and 51 nozzle diameters downstream. Both pdfs are close to Gaussian. At the more downstream position the pdf variance is less as the turbulence kinetic energy decreases. The statistics are effectively Eulerian statistics i.e., dependent upon the particle being at some particular axial location. The data could also be presented in a purely Lagrangian fashion by analyzing the results as functions of the time-of-flight for each droplet.

### 3.3 Analysis of measurement uncertainty

The random signal noise affecting the measurements is due to pmt dark noise, laser noise, fluctuations in stray light intensity arriving at the pmt, electronic noise, and discretization error. The discretization error is  $\pm 1$  count which corresponds to  $\pm 2.4$  mV for our 12 bit analog to digital converter. With the laser off, the rms noise on each signal has been measured to be 1.3 mV with the pmt cathode voltage set at  $-800$  V (same as for data collection). This measurement includes contributions from pmt dark noise and electronic noise. With the laser power on, the rms noise is 9.6 mV. A typical signal for a  $69 \mu\text{m}$  hexadecane droplet is 1 V peak on each of the four channels giving a peak signal

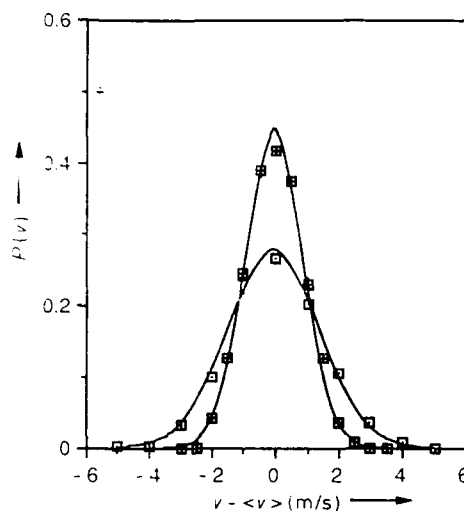


Fig. 6. Velocity probability density functions at  $z = D = 27$  and  $51$ .  $\square$   $z = D = 27$ ,  $\boxplus$   $z = D = 51$

to noise ratio of  $\sim 100$ . The peak signal strength depends quadratically on particle diameter. Therefore, a  $35 \mu\text{m}$  droplet would provide approximately four times less signal. The signal to noise ratio can be improved by increasing the laser power and by decreasing the background scattered light.

The effect of noise on the pmt signals gives rise to uncertainty in the position and velocity measurements. As the droplet passes through the sheet of light, a minimum of 3 useful data samples along a pulse are obtained (for which the total pmt signal is greater than 20% of its measured maximum value). This leads to at least three values of  $X$  to be averaged to determine the droplet displacement and three points for the Gaussian curve fit for velocity. Additional data can be obtained by increasing the data collection rate above 20 kHz.

Precision of the position measurements has been estimated for typical experimental conditions at an axial location of  $z = D = 27$ . At this position, the droplet mean axial velocity is 10.5 m/s. The average number of useful data points along a pmt pulse at this velocity is 3.4 and the average variance of the  $x$  or  $y$  position obtained from the groups of 3 or 4 data points was  $0.35 \text{ mm}^2$ . If it is assumed that the error in position measurement from the true position is normally distributed and the droplets are passing vertically through the sheet (no change in radial position), the uncertainty in the mean value for displacement is  $\pm 0.3 \text{ mm}$ . (The latter assumption suggests the uncertainty should be less than 0.3 mm because some droplets may possess a radial velocity within the laser sheet.) Accuracy of the position measurements is ensured by calibrating just prior to data collection using 60 droplets and then averaging at each calibration point.

The precision of the velocity measurements can be inferred by injecting droplets into a 10.5 m/s laminar flow and measuring the rms velocity fluctuation. The mean droplet velocity and true rms are measured using two sheets of laser light and a 100 kHz transient recorder. The true rms velocity

was 0.2 m/s (1.9% of the mean) and the value obtained using one sheet and the Gaussian curve fitting technique was 0.34 m/s (3.2%), providing an indication of the precision of this approach.

#### 4 Results and discussion

The radial dispersion of the droplets can be analyzed in either purely Eulerian terms or Lagrangian terms. The Eulerian dispersion of droplets is shown in Fig. 7 as a function of the axial location. The dispersion increases quite rapidly for  $z/D$  greater than about 30. The time-of-flight measurements have been ensemble averaged and are shown in Fig. 8. The quadratic dependence of time-of-flight on axial position is consistent with that expected for a round jet.

With the time for each droplet's flight known we are in a position to present truly Lagrangian statistics for particle dispersion in a turbulent jet. This is achieved by taking data at many finely spaced axial locations along the jet. We then analyze the entire data set and sort it into narrow bins of time. The results are shown in Fig. 9. For this plot, a data set was collected at intervals of  $1.4 z/D$ . The entire set was re-sorted into bins of time; the width of each bin was  $\Delta t/t \leq \pm 0.04$ .

By combining the data of Figs. 7 and 8, the Eulerian dispersion data can provide a quasi-Lagrangian result that is a function of mean time-of-flight rather than position (also shown on Fig. 9). The "mean" refers to an average at each axial location. As can be seen in Fig. 9, for our experimental conditions the results overlap. The practice of deriving Lagrangian statistics from essentially Eulerian measurements was used by Vames and Hanratty (1988) and is valid under certain conditions. For systems in which the particle velocity fluctuation is negligible relative to its mean axial velocity, the times-of-flight pdf at a given axial location will approach a delta function. For these systems the mean time-of-flight approach provides an excellent approximation to the true Lagrangian measurement.

In the current experiment we have measured a time-of-flight pdf that exhibits some significant spread as shown in Fig. 10. The pdf appears to be log-normal; this may be due to the fact that the time-of-flight is a bounded stochastic variable i.e., it cannot be less than zero. Based on this observation, one would not necessarily expect the two data sets of Fig. 9 to overlap.

The experimental approach reported here collects independent samples of  $x$ ,  $y$ ,  $z$  and  $t$  allowing  $\sigma_x^2(t)$  and  $\sigma_z^2(z)$  (or  $\langle t \rangle$ ) to be considered separately. The results will necessarily converge when the variance in time-of-flight  $t$  at a fixed axial location  $z$  approaches zero. However, a positive variance does not necessarily imply  $\sigma_x^2(t)$  will not be numerically equal to  $\sigma_z^2(\langle t \rangle)$ , but the accuracy of the approximation is dubious. Fundamentally, the assumption is unjustified although in practice the measurements of an averaged quantity such as particle dispersion may not be strongly affected.

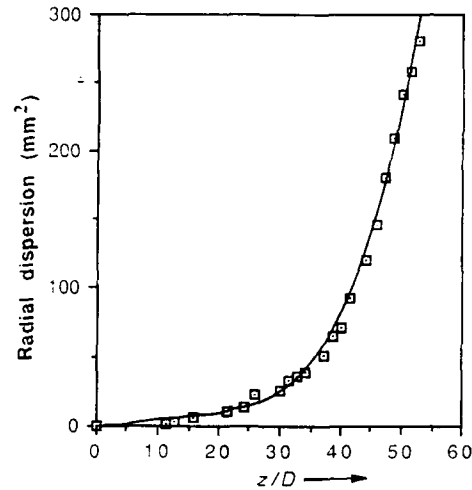


Fig. 7. Radial dispersion measurements as a function of axial distance

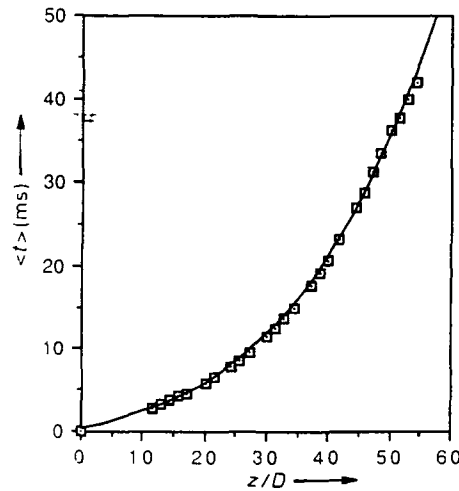


Fig. 8. Mean time-of-flight measurements for 69  $\mu\text{m}$  hexadecane droplets

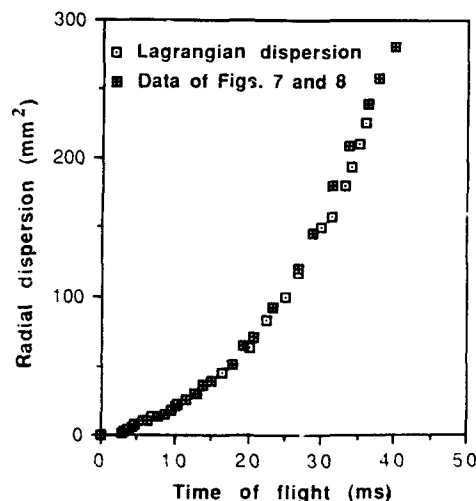


Fig. 9. Lagrangian measurements of radial dispersion

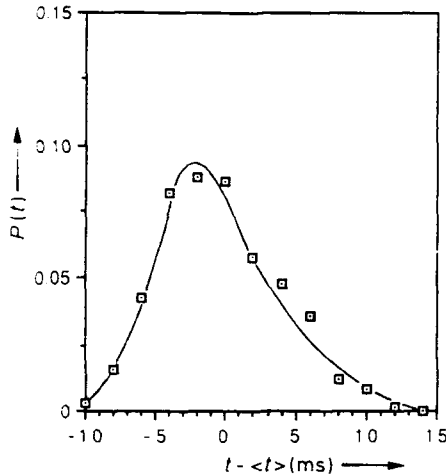


Fig. 10. Time-of-flight pdf for  $z/D = 51$

This behavior is evident in our data and presumably also is true for the data of Vames and Hanratty (1988).

By thickening the laser sheet to follow the droplet motion over a longer time or using multiple sheets, it should be possible to directly obtain particle Lagrangian velocity correlations and time scales similar to the measurements by Snyder and Lumley (1971). This approach avoids the empirical uncertainties involved when inferring Lagrangian time scales from Eulerian measurements (Vames and Hanratty 1988, Wells and Stock 1983, and Hardalupas et al. 1989). Because of the sensitivity of the photomultiplier detector we anticipate being able to perform the experiment on microballoons or hollow glass spheres which can follow the flow faithfully. By this means it should be possible to measure Lagrangian statistics of fluid particles in a shear flow. These results would carry considerable importance in the general area of turbulent dispersion.

## 5 Conclusions

A technique has been developed which facilitates the collection of statistically large samples of particle motion. The methodology yields particle dispersion and velocity statistics

directly, in comparison to the time intensive data reduction and analysis which characterize photo and video imaging methods. The statistics can be cast in a form which is truly Lagrangian in nature since individual particles have been tracked from a known initial location and their time-of-flight is measured. For the particle and flow scales of this experiment it was found that an average time-of-flight analysis provides close agreement to the true Lagrangian time-of-flight measurements for dispersion calculations. Since the technique is non-intrusive, it can be used in a wide range of flow conditions and configurations including dilute combusting sprays.

## Acknowledgements

This material is based upon work supported by the U.S. Air Force Office of Scientific Research under Award No. AFOSR-89-0392.

## References

- Batchelor, G. K. 1957: Diffusion in free turbulent shear flows. *J. Fluid Mech.* 3, 67-80
- Friedlander, S. K. 1957: Behavior of suspended particles in a turbulent fluid. *A.I.Ch.E. J.* 3, 381
- Hardalupas, Y.; Taylor, A. M. K. P.; Whitlaw, J. H. 1989: Velocity and particle-flux characteristic of turbulent particle-laden jets. *Proc. R. Soc. Lond. A* 426, 31-78
- Lee, M. M.; Hanratty, T. J.; Adrian, R. J. 1988: An axial viewing photographic technique to study turbulence characteristics of particles. *Int. J. Multiphase Flow* 15, 787-802
- Reeks, M. W. 1977: On the dispersion of small particles suspended in an isotropic turbulent field. *J. Fluid Mech.* 83, 41
- Saffman, P. G. 1960: On the effect of molecular diffusivity in turbulent diffusion. *J. Fluid Mech.* 8, 273-283
- Snyder, W. H.; Lumley, J. L. 1971: Some measurements of particle velocity autocorrelation functions in a turbulent flow. *J. Fluid Mech.* 48, 41-71
- Taylor, G. I. 1921: Diffusion by continuous movements. *Proc. Lond. Math. Soc.* 20, 196
- Vames, J. S.; Hanratty, T. J. 1988: Turbulent dispersion of droplets for air flow in a pipe. *Exp. Fluids* 6, 94-104
- Wells, M. R.; Stock, D. E. 1983: The effects of crossing trajectories on the dispersion of particles in a turbulent flow. *J. Fluid Mech.* 136, 31-62

Received May 3, 1991

2T-0  
and 70  
of pure

(001)

SECRET  
NOFORN  
UNCLASSIFIED